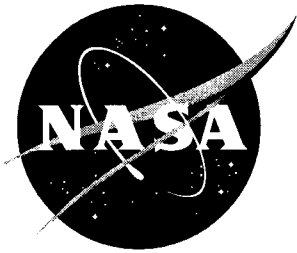


NASA/TM-2003-212165



Electromagnetic Scattering From a Polygonal Thin Metallic Plate Using Quadrilateral Meshing

Manohar D. Deshpande
Langley Research Center, Hampton, Virginia

May 2003

The NASA STI Program Office . . . in Profile

Since its founding, NASA has been dedicated to the advancement of aeronautics and space science. The NASA Scientific and Technical Information (STI) Program Office plays a key part in helping NASA maintain this important role.

The NASA STI Program Office is operated by Langley Research Center, the lead center for NASA's scientific and technical information. The NASA STI Program Office provides access to the NASA STI Database, the largest collection of aeronautical and space science STI in the world. The Program Office is also NASA's institutional mechanism for disseminating the results of its research and development activities. These results are published by NASA in the NASA STI Report Series, which includes the following report types:

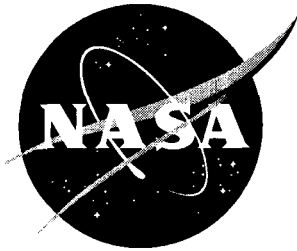
- **TECHNICAL PUBLICATION.** Reports of completed research or a major significant phase of research that present the results of NASA programs and include extensive data or theoretical analysis. Includes compilations of significant scientific and technical data and information deemed to be of continuing reference value. NASA counterpart of peer-reviewed formal professional papers, but having less stringent limitations on manuscript length and extent of graphic presentations.
- **TECHNICAL MEMORANDUM.** Scientific and technical findings that are preliminary or of specialized interest, e.g., quick release reports, working papers, and bibliographies that contain minimal annotation. Does not contain extensive analysis.
- **CONTRACTOR REPORT.** Scientific and technical findings by NASA-sponsored contractors and grantees.
- **CONFERENCE PUBLICATION.** Collected papers from scientific and technical conferences, symposia, seminars, or other meetings sponsored or co-sponsored by NASA.
- **SPECIAL PUBLICATION.** Scientific, technical, or historical information from NASA programs, projects, and missions, often concerned with subjects having substantial public interest.
- **TECHNICAL TRANSLATION.** English-language translations of foreign scientific and technical material pertinent to NASA's mission.

Specialized services that complement the STI Program Office's diverse offerings include creating custom thesauri, building customized databases, organizing and publishing research results ... even providing videos.

For more information about the NASA STI Program Office, see the following:

- Access the NASA STI Program Home Page at <http://www.sti.nasa.gov>
- E-mail your question via the Internet to help@sti.nasa.gov
- Fax your question to the NASA STI Help Desk at (301) 621-0134
- Phone the NASA STI Help Desk at (301) 621-0390
- Write to:
NASA STI Help Desk
NASA Center for AeroSpace Information
7121 Standard Drive
Hanover, MD 21076-1320

NASA/TM-2003-212165



Electromagnetic Scattering From a Polygonal Thin Metallic Plate Using Quadrilateral Meshing

Manohar D. Deshpande
Langley Research Center, Hampton, Virginia

National Aeronautics and
Space Administration

Langley Research Center
Hampton, Virginia 23681-2199

May 2003

Contents

List of Symbols	iv
List of Figures	v
Abstract	1
1.0 INTRODUCTION	1
2.0 THEORY	3
Scattered Far Field	9
3.0 NUMERICAL RESULTS	10
RCS of Hexagonal Plate	10
RCS of Equilateral Triangular Plate	15
RCS of Equilateral Triangular Plate with Concentric Equilateral Hole	19
RCS of Diamond Shaped Plate	24
4.0 CONCLUSION	28
APPENDIX A	28
REFERENCES	30

List of Symbols

$A_{ij}^{m,n}$	ij^{th} element of matrix due to m^{th} and n^{th} quadrilateral patches.
A_x, A_y	x- and y- components of magnetic vector potential \vec{A}
\vec{A}_{ni}	Magnetic vector potential due to i^{th} edge on n^{th} quadrilateral patch.
\vec{A}	Magnetic vector potential.
\vec{B}_{ni}	Basis function for i^{th} edge of n^{th} quadrilateral patch.
ds_n, ds_m	Elementary area on n^{th} and m^{th} patches respectively.
$\det[J]$	Determinant of Jacobian for coordinate transformation
\vec{E}_{in}	Incident electric field
E_{θ_i}	Theta component of incident electric field
E_{ϕ_i}	Phi component of incident electric field.
E_{xi}, E_{yi}, E_{zi}	x-,y-, and z-components of incident electric field.
\vec{E}_s, \vec{H}_s	Electric and magnetic scattered field.
E_{θ}, E_{ϕ}	Theta and phi components of electric far field.
EM	Electromagnetics
EFIE	Electric Field Integral Equation
ESP	Electromagnetic Surface Patch Code
\vec{H}_{in}	Incident magnetic field
\vec{J}	Surface electric current density.
\vec{k}_i	Vector wavenumber in direction on incidence angle
k_0	Free space wave number
$l_i, i = 1,2,3,4$	Length of four sides of quadrilateral patch
MoM	Method of Moments
N	Total number of quadrilateral patches.
$N_i(\xi, \eta)$	Linear transformation function.
PoMePl	Polygonal Metallic Plate Code
RWG	Rao Wilton Glisson triangular basis function
\vec{r}	Position vector for observation point
\vec{r}'	Position vector for source point
T_{ni}	Complex number representing amplitudes of edge currents
$[T]$	Column matrix representing amplitudes of edge currents
$[V]$	Column matrix representing incident wave values.
$\hat{x}, \hat{y}, \hat{z}$	Unit vectors along x-, y-, and z-axes
x_i, y_i	i^{th} node coordinates

$[Z]$	Impedance square matrix
α_0	Angle = 90 (degrees) for E-polarization and equal to 0 for H-polarization
ϵ_0, μ_0	Permittivity and permeability of free space medium
η_0	Free space impedance equal to 120π
ω	Radian frequency $2\pi f$
$\hat{\theta}, \hat{\phi}$	Unit vectors along theta and phi directions
ϕ	Scalar Potential
∇	Gradient operator
$\sigma_{EE}, \sigma_{HH}, \sigma_{EH}, \sigma_{HE}$	RCS in dB-m ²

List of Figures

- Figure 1 Geometry of arbitrarily shaped thin metallic plate in x-y plane and illuminated by a plane wave.
- Figure 2 Arbitrarily shaped thin metallic plate discretized into quadrilaterals, m^{th} and n^{th} are typical elements with their four nodes.
- Figure 3 (a) n^{th} quadrilateral in x-y plane, (b) n^{th} quadrilateral in ξ, η plane
- Figure 4 (a) n^{th} quadrilateral with four edges, (b) and its adjacent quadrilateral.
- Figure 5 Thin metallic flat plate of hexagonal shape with $a = 2.074$ cm and discretized into quadrilateral patches.
- Figure 6 Monostatic RCS of hexagonal plate (shown in Figure 5) when illuminated by E-polarized plane wave for various discretizations, frequency = 11.811GHz.
- Figure 7 Monostatic RCS of hexagonal plate (shown in Figure 5) when illuminated by H-polarized plane wave for various discretizations, frequency = 11.811GHz.
- Figure 8 Monostatic RCS of hexagonal plate (shown in Figure 5) when illuminated by E-polarized plane wave $\alpha_0 = 90^\circ$ at $\phi_i = -90^\circ$ and $\phi_i = 90^\circ$, solid line- present method, dashed line RWG functions, solid square symbol-measurement, frequency = 11.811GHz.
- Figure 9 Monostatic RCS of hexagonal plate (shown in Figure 5) when illuminated by H-polarized plane wave $\alpha_0 = 0^\circ$ at $\phi_i = -90^\circ$ and $\phi_i = 90^\circ$, solid line- present method, dashed dot line ESP-code, solid square symbol-measurement, and dashed line RWG function, frequency = 11.811GHz.
- Figure 10 Monostatic RCS of hexagonal plate (shown in Figure 5) when illuminated by H-polarized plane wave $\alpha_0 = 0^\circ$ at $\phi_i = 0^\circ$ and $\phi_i = 180^\circ$, solid line-

present method, dashed dot line ESP-code, solid square symbol-measurement, and dashed line RWG function, frequency = 11.811GHz.

- Figure 11 Monostatic RCS of hexagonal plate (shown in Figure 5) when illuminated by E-polarized plane wave $\alpha_0 = 90^\circ$ at $\phi_i = 0^\circ$ and $\phi_i = 180^\circ$, solid line-present method, dashed line RWG functions, solid square symbol-measurement, frequency = 11.811GHz.
- Figure 12 Equilateral triangular thin metallic flat plate with $a = 5.08$ cm and descritized into quadrilateral patches.
- Figure 13 Monostatic RCS of equilateral triangular plate (shown in Figure 12) when illuminated by E-polarized plane wave $\alpha_0 = 90^\circ$ at $\phi_i = 0^\circ$ and $\phi_i = 180^\circ$, solid line- present method, short dashed line- RWG functions, long dashed line ESP-code, solid square symbol- measurement, frequency = 11.811GHz.
- Figure 14 Monostatic RCS of equilateral triangular plate (shown in Figure 12) when illuminated by H-polarized plane wave $\alpha_0 = 0^\circ$ at $\phi_i = 0^\circ$ and $\phi_i = 180^\circ$, solid line- present method, short dashed line- RWG functions, dashed dot line ESP-code, solid square symbol- measurement, frequency = 11.811GHz
- Figure 15 Monostatic RCS of equilateral triangular plate (shown in Figure 12) when illuminated by E-polarized plane wave $\alpha_0 = 90^\circ$ at $\phi_i = -90^\circ$ and $\phi_i = 90^\circ$, solid line- present method, short dashed line- RWG functions, dashed dot line ESP-code, frequency = 11.811GHz
- Figure 16 Monostatic RCS of equilateral triangular plate (shown in Figure 12) when illuminated by H-polarized plane wave $\alpha_0 = 0^\circ$ at $\phi_i = -90^\circ$ and $\phi_i = 90^\circ$, solid line- present method, short dashed line- RWG functions, dashed dot line ESP-code, solid square symbol- measurement , frequency = 11.811GHz.
- Figure 17 Monostatic RCS of equilateral triangular plate (shown in Figure 12) when illuminated by E-polarized plane wave $\alpha_0 = 90^\circ$ as a function of ϕ_i for frequency = 11.811 GHz, $\theta_i = 90^\circ$. solid line- present method, short dashed line- RWG functions, dashed dot line ESP-code, frequency = 11.811GHz.

- Figure 18 Monostatic RCS of equilateral triangular plate (shown in Figure 12) when illuminated by E-polarized plane wave $\alpha_0 = 90^\circ$ as a function of frequency for $\phi_i = 90$ and $\theta_i = 90^\circ$. solid line- present method, short dashed line- RWG functions, dashed dot line ESP-code, solid square symbols- measurement.
- Figure 19 Equilateral triangular thin metallic flat plate with a concentric equilateral triangular hole, $a = 5.08$ cm, $b = 2.54$ cm and discretized into quadrilateral patches.
- Figure 20 Monostatic RCS of equilateral triangular plate with equilateral triangular hole (shown in Figure 19) when illuminated by E-polarized plane wave $\alpha_0 = 90^\circ$ at $\phi_i = -90^\circ$ and $\phi_i = 90^\circ$, solid line- present method, short dashed line- RWG functions, dashed dot line ESP-code, solid square symbols- measurement, frequency = 11.811GHz.
- Figure 21 Monostatic RCS of equilateral triangular plate with equilateral triangular hole (shown in Figure 19) when illuminated by H-polarized plane wave $\alpha_0 = 0^\circ$ at $\phi_i = -90^\circ$ and $\phi_i = 90^\circ$, solid line- present method, short dashed line- RWG functions, dashed dot line ESP-code, solid square symbols- measurement, frequency = 11.811GHz.
- Figure 22 Monostatic RCS of equilateral triangular plate with equilateral triangular hole (shown in Figure 19) when illuminated by E-polarized plane wave $\alpha_0 = 90^\circ$ at $\phi_i = 0^\circ$ and $\phi_i = 180^\circ$, solid line- present method, short dashed line- RWG functions, dashed dot line ESP-code, solid square symbols- measurement, frequency = 11.811GHz.
- Figure 23 Monostatic RCS of equilateral triangular plate with equilateral triangular hole (shown in Figure 19) when illuminated by H-polarized plane wave $\alpha_0 = 0^\circ$ at $\phi_i = 0^\circ$ and $\phi_i = 180^\circ$, solid line- present method, short dashed line- RWG functions, dashed dot line ESP-code, solid square symbols- measurement, frequency = 11.811GHz.
- Figure 24 Monostatic RCS of equilateral triangular plate with equilateral triangular hole (shown in Figure 19) when illuminated by E-polarized plane wave $\alpha_0 = 90^\circ$ as a function of ϕ_i for frequency = 11.811 GHz, $\theta_i = 90^\circ$. solid line- present method, short dashed line- RWG functions, dashed dot line ESP-code, solid square symbols- measurement, frequency = 11.811GHz.
- Figure 25 Monostatic RCS of equilateral triangular plate with equilateral triangular hole (shown in Figure 19) when illuminated by E-polarized plane wave $\alpha_0 = 90^\circ$ as a function of frequency for $\phi_i = -90$ and $\theta_i = 90^\circ$ (grazing incidence at edge). solid line- present method, short dashed line- RWG functions, dashed dot line ESP-code, solid square symbols- measurement.

- Figure 26 Monostatic RCS of equilateral triangular plate with equilateral triangular hole (shown in Figure 19) when illuminated by E-polarized plane wave $\alpha_0 = 90^\circ$ as a function of frequency for $\phi_i = 90^\circ$ and $\theta_i = 90^\circ$ (grazing incidence at tip). solid line- present method, short dashed line- RWG functions, dashed dot line ESP-code, solid square symbols- measurement.
- Figure 27 Thin, metallic diamond-shaped flat plate with $a = 3.592$ cm and discretized into quadrilateral patches.
- Figure 28 Monostatic RCS of diamond-shaped plate (shown in Figure 27) when illuminated by H-polarized plane wave $\alpha_0 = 0^\circ$ at $\phi_i = 90^\circ$ and $\phi_i = -90^\circ$, solid line- present method, short dashed line- RWG functions, dashed dot line ESP-code, solid square symbols- measurement, frequency = 11.811GHz.
- Figure 29 Monostatic RCS of diamond-shaped plate (shown in Figure 27) when illuminated by E-polarized plane wave $\alpha_0 = 90^\circ$ at $\phi_i = 90^\circ$ and $\phi_i = -90^\circ$, solid line- present method, short dashed line- RWG functions, dashed dot line ESP-code, solid square symbols- measurement, frequency = 11.811GHz.
- Figure 30 Monostatic RCS of diamond-shaped plate (shown in Figure 27) when illuminated by H-polarized plane wave $\alpha_0 = 0^\circ$ at $\phi_i = 0^\circ$ and $\phi_i = 180^\circ$, solid line- present method, short dashed line- RWG functions, dashed dot line ESP-code, frequency = 11.811GHz.
- Figure 31 Monostatic RCS of diamond-shaped plate (shown in Figure 27) when illuminated by E-polarized plane wave $\alpha_0 = 90^\circ$ at $\phi_i = 0^\circ$ and $\phi_i = 180^\circ$, solid line- present method, short dashed line- RWG functions, dashed dot line ESP-code, solid square symbols- measurement, frequency = 11.811GHz.
- Figure 32 Monostatic RCS of diamond-shaped plate (shown in Figure 27) when illuminated by E-polarized plane wave $\alpha_0 = 90^\circ$ as a function of ϕ_i for frequency = 11.811 GHz, $\theta_i = 90^\circ$. solid line- present method, short dashed line- RWG functions, dashed dot line ESP-code, solid square symbols- measurement, frequency = 11.811GHz.

ABSTRACT

The problem of electromagnetic (EM) scattering from irregularly shaped, thin, metallic flat plates in free space is solved using the electric field integral equation (EFIE) approach in conjunction with the method of moments (MoM) with quadrilateral meshing. An irregularly shaped thin plate is discretized into quadrilateral patches and the unknown electric surface current over the plate is expressed in terms of proper basis functions over these patches. The basis functions for the electric surface current density that satisfy the proper boundary conditions on these quadrilateral patches are derived. The unknown surface current density on these quadrilateral patches is determined by setting up and solving the electric field integral equation by the application of the MoM. From the knowledge of the surface current density, the EM scattering from various irregularly shaped plates is determined and compared with the earlier published results. The novelty in the present approach is the use of quadrilateral patches instead of well known and often used triangular patches. The numerical results obtained using the quadrilateral patches compare favorably with measured results.

1. INTRODUCTION

The EM scattering from a complex-shaped metallic object is of practical interest to electromagnetic analysts as well as to engineers. The EM scattering from polygonal shaped plates is of special interest because a complex-shaped object can always be modeled as an interconnection of these polygonal flat plates. An EM scattering analysis of polygonal shaped metallic plates can be accomplished by using various numerical techniques [1-4]. One of the widely used techniques is the MoM in which a polygonal plate is first discretized into number of triangular patches called sub domains. The unknown surface current density on these sub

domains is then expressed in terms of well known Rao-Wilton-Glisson (RWG) [3] basis functions. The unknown surface current density on these sub domains is then determined using the EFIE in conjunction with the MoM. Although the triangular meshing and use of RWG basis functions is a very popular and mature concept, the non-vanishing normal component of surface current on one of the inclined edges of sub-domain triangles attached to the open /boundary edge of polygonal plate will give a non-zero normal component of the surface current. However, the non-zero normal component of the surface current on the boundary edge will approach zero when very fine discretization is used in the region close to the open/boundary edges. This problem will not arise if one uses a sub domain element (near the boundary) whose edges will be either along the boundary or normal to the boundary (such as quadrilateral element). Another approach as implemented in [4] divides a polygonal plate into small rectangles. The surface current density over each sub domain is expressed in terms of overlapping triangular functions (roof-top functions) in the direction of current flow and a pulse function in the orthogonal direction. The EFIE in conjunction with the MoM is then used to determine the surface current density. An important advantage of this procedure is that the impedance matrix encountered in this procedure has a block Toeplitz nature, a property that is useful in reducing the matrix filling time. However, the major drawback of this scheme is that the curve boundaries are approximated by stair cases and hence for accurate results requires very fine discretization.

In this report the problem of electromagnetic scattering of plane waves by an arbitrarily shaped, thin metallic plate is studied using the EFIE method in conjunction with quadrilateral meshing. Use of the equivalence principle and the free space Green's function in deriving the EFIE with the surface current density as an unknown is described in detail. With proper choice of the expansion and testing functions over the quadrilateral mesh, the MoM is described to

convert the EFIE into a matrix equation. The procedure to obtain the scattered far field by the plate in terms of the electric surface current is also described.

The remainder of report is organized as follows. The formulation of the problem in terms of the EFIE using the surface equivalence principle is developed in section 2. Numerical results on the mono-static radar cross section of various polygonal shaped metallic plates are presented in section 3 and compared with earlier published data. The advantages and limitations of the present formulation are discussed in section 4.

2. THEORY

Consider a time harmonic electromagnetic plane wave incident on an irregularly shaped, infinitesimally thin metallic plate as shown in Figure 1. The incident field with a time dependence $e^{j\omega t}$ may be written as

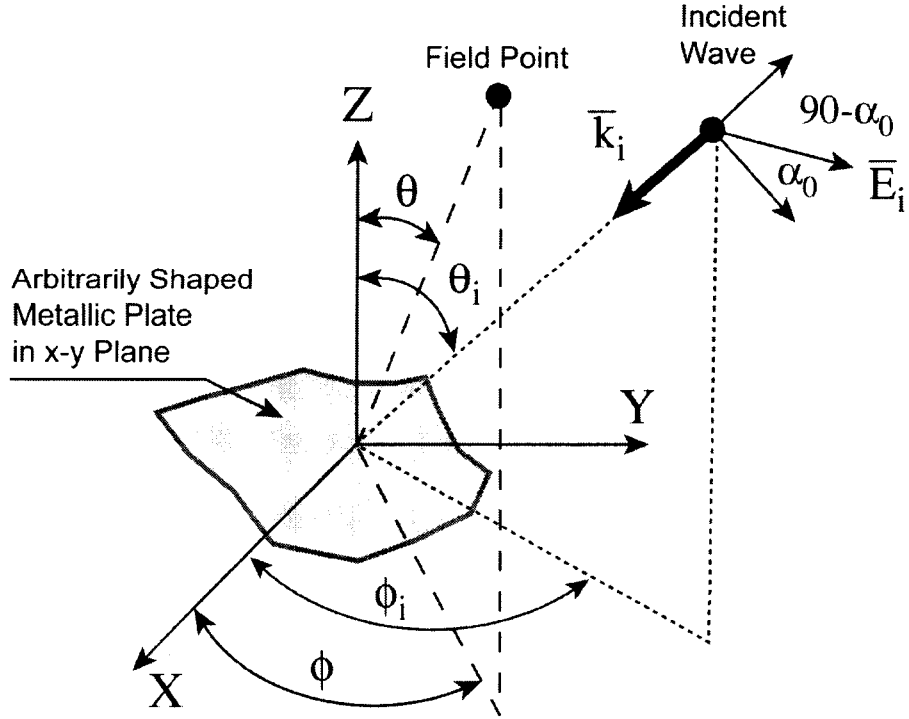


Figure 1: Geometry of arbitrarily shaped thin metallic plate in x-y plane and illuminated by a plane wave

$$\vec{E}_{in} = (\hat{\theta}E_{\theta_i} + \hat{\phi}E_{\phi_i})e^{-j\vec{k}_i \cdot \vec{r}} \quad (1)$$

where $\vec{k}_i = -k_0[\hat{x}\cos(\phi_i)\sin(\theta_i) + \hat{y}\sin(\phi_i)\sin(\theta_i) + \hat{z}\cos(\theta_i)]$, $\vec{r} = \hat{x}x + \hat{y}y + \hat{z}z$,

$E_{\theta_i} = |\vec{E}_i|\cos(\alpha_0)$, and $E_{\phi_i} = |\vec{E}_i|\sin(\alpha_0)$, k_0 being the free-space wave number. With

reference to Figure 1, $\alpha_0 = 0$ corresponds to H-polarization and $\alpha_0 = 90^\circ$ corresponds to E-

polarization. From equation (1), the x-, y-, and z-components of the incident field may be written, respectively, as

$$E_{xi} = E_{\theta_i}\cos(\theta_i)\cos(\phi_i) - E_{\phi_i}\sin(\phi_i) \quad (2)$$

$$E_{yi} = E_{\theta_i}\cos(\theta_i)\sin(\phi_i) - E_{\phi_i}\cos(\phi_i) \quad (3)$$

$$E_{zi} = -E_{\theta_i}\sin(\theta_i) \quad (4)$$

The corresponding magnetic field components are obtained through

$$\vec{H}_{in} = \frac{1}{k_0\eta_0}\vec{k}_i \times \vec{E}_{in} \quad (5)$$

where η_0 is the free-space impedance. The incident field with $E_{\theta_i} \neq 0$ and $E_{\phi_i} = 0$ is called the H-polarized wave and $E_{\theta_i} = 0$ and $E_{\phi_i} \neq 0$ is called the E-polarized wave.

To facilitate the solution of the problem using the equivalence principle, the thin metallic plate is replaced by the equivalent electric surface current density $\vec{J}(x, y)$. The scattered field due to \vec{J} may be obtained through the vector magnetic potentials as

$$\vec{E}_s(\vec{J}) = -j\omega\vec{A} - \nabla\phi \quad (6)$$

$$\vec{H}_s(\vec{J}) = \frac{1}{\mu_0} \nabla \times \vec{A} \quad (7)$$

where the magnetic vector and scalar potentials are given by

$$\vec{A} = \frac{\mu_0}{4\pi} \int_S \vec{J} \frac{e^{-jk_0|\vec{r}-\vec{r}'|}}{|\vec{r}-\vec{r}'|} ds \quad (8)$$

$$\phi = \frac{j}{4\pi\omega\epsilon_0} \int_S (\nabla \cdot \vec{J}) \frac{e^{-jk_0|\vec{r}-\vec{r}'|}}{|\vec{r}-\vec{r}'|} ds \quad (9)$$

where ϵ_0 and μ_0 are the permittivity and permeability, respectively, of free-space, \vec{r} and \vec{r}' are respectively the coordinates of field and source points. From the knowledge of the scattered field and incident field, the EFIE is set up by equating the total tangential electric field over the surface of the polygonal plate to zero. Hence

$$[j\omega\vec{A} + \nabla\phi]_{\tan} = [\vec{E}_{in}]_{\tan} \quad (10)$$

To determine the approximate solution of the integral equation in (10) using the MoM, the polygonal surface is approximated by a union of quadrilaterals as shown in Figure 2. On the n^{th} quadrilateral the electric surface current density can be represented by a superposition of vector functions $\vec{B}_{ni}(x, y)$ as

$$\vec{J}_n(x, y) = \sum_{i=1}^4 T_{ni} \vec{B}_{ni}(x, y) \quad (11)$$

where T_{ni} is the amplitude of electric current normal to the i^{th} edge of the n^{th} element

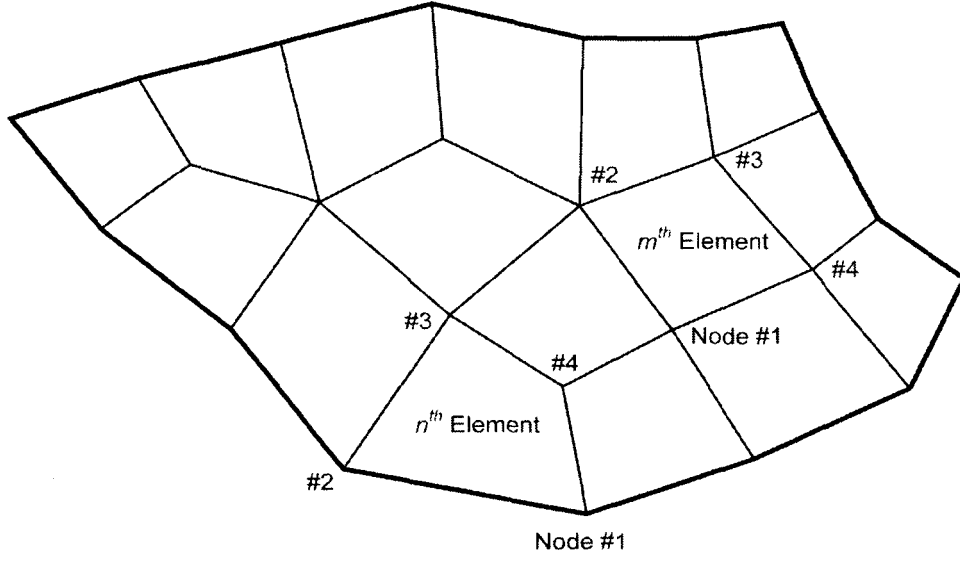


Figure 2: Arbitrarily shaped thin metallic plate discretized into quadrilaterals. m^{th} and n^{th} are typical elements with their four nodes

(as shown in Figure 4). The vector basis function $\bar{B}_{ni}(x, y)$ representing the surface current density on the n^{th} quadrilateral is required to satisfy the appropriate boundary conditions; such as the normal component of $\bar{B}_{ni}(x, y)$ to the i^{th} edge must be unity, and must have a value of zero on the other remaining edges. Construction of such a vector basis function with help of Figure 3 is explained in detail in the Appendix A.

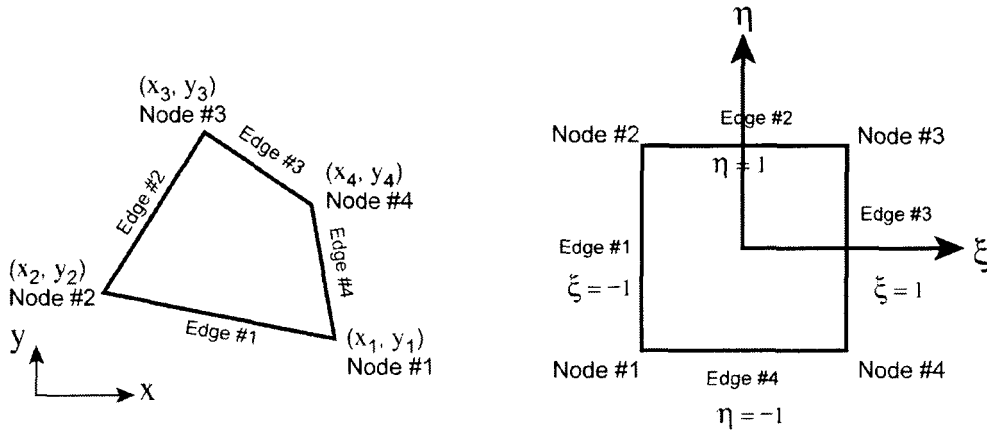


Figure 3: (a) n^{th} quadrilateral in x-y plane, (b) n^{th} quadrilateral in ξ, η plane

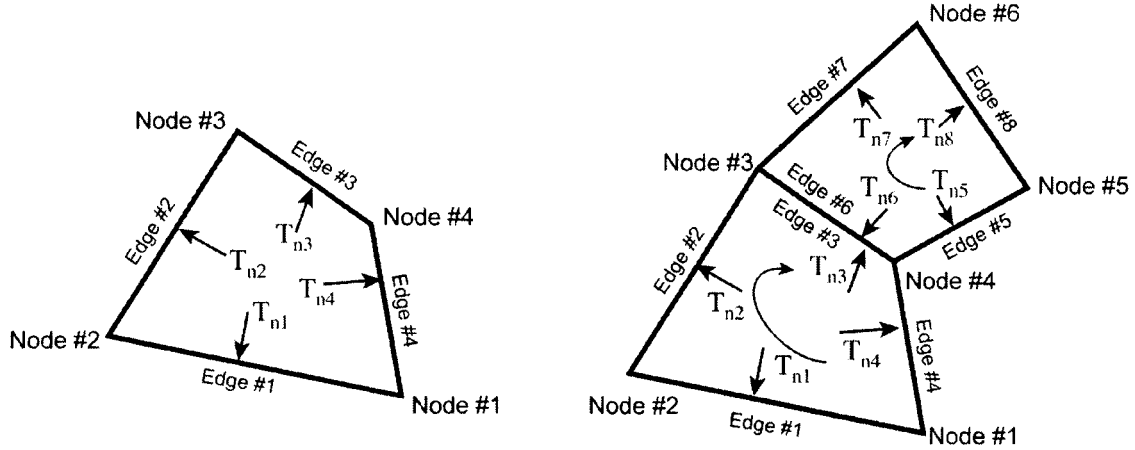


Figure 4: (a) n^{th} quadrilateral with four edges, (b) n^{th} and its adjacent quadrilateral

$$\left[\sum_{n=1}^N \sum_{i=1}^4 T_{ni} (j\omega \vec{A}_{ni} + \nabla \phi_{ni}) \right]_{\tan} = [\vec{E}_{in}]_{\tan} \quad (12)$$

where \vec{A}_{ni} and ϕ_{ni} are obtained from equations (8) and (9), respectively, by replacing \vec{J} by \vec{B}_{ni} . Selecting \vec{B}_{mj} with $j = 1, 2, 3, 4$ and $m = 1, 2, 3, \dots, N$ as a testing function and application of the MoM to equation (12) yields

$$\sum_{n=1}^N \sum_{i=1}^4 T_{ni} \left(\frac{-j\omega\mu_0}{4\pi} \iint_n \vec{B}_{ni} ds_n \bullet \iint_m \vec{B}_{mj} \frac{e^{-jk_0|\vec{r}-\vec{r}'|}}{|\vec{r}-\vec{r}'|} ds_m + \right. \\ \left. \frac{j}{4\pi\omega\epsilon_0} \iint_n \nabla \bullet \vec{B}_{ni} ds_n \iint_m \nabla \bullet \vec{B}_{mj} \frac{e^{-jk_0|\vec{r}-\vec{r}'|}}{|\vec{r}-\vec{r}'|} ds_m \right) = - \iint_m \vec{B}_{mj} \bullet [\vec{E}_{in}]_{\tan} ds_m \quad (13)$$

The left side of equation (13) over the n^{th} quadrilateral (Figure 4(a)) can be written as

$$\begin{bmatrix} A_{11}^{n,n} & A_{12}^{n,n} & A_{13}^{n,n} & A_{14}^{n,n} \\ A_{21}^{n,n} & A_{22}^{n,n} & A_{23}^{n,n} & A_{24}^{n,n} \\ A_{31}^{n,n} & A_{32}^{n,n} & A_{33}^{n,n} & A_{34}^{n,n} \\ A_{41}^{n,n} & A_{42}^{n,n} & A_{43}^{n,n} & A_{44}^{n,n} \end{bmatrix} \begin{bmatrix} T_{n1} \\ T_{n2} \\ T_{n3} \\ T_{n4} \end{bmatrix} \quad (14)$$

where

$$A_{ij}^{n,n} = \left(\frac{-j\omega\mu_0}{4\pi} \int_n \bar{B}_{ni} ds_n \bullet \int_m \bar{B}_{mj} \frac{e^{-jk_0|\bar{r}-\bar{r}'|}}{|\bar{r}-\bar{r}'|} ds_m + \right. \\ \left. \frac{j}{4\pi\omega\epsilon_0} \int_n \nabla \bullet \bar{B}_{ni} ds_n \int_m \nabla \bullet \bar{B}_{mj} \frac{e^{-jk_0|\bar{r}-\bar{r}'|}}{|\bar{r}-\bar{r}'|} ds_m \right) \quad (15)$$

Now consider union of two adjacent quadrilaterals with a common edge as shown in Figure

4(b). The left side of equation (13) for two adjacent quadrilaterals can be written as

$$\begin{bmatrix} A_{11}^{n,n} & A_{12}^{n,n} & (A_{13}^{n,n} - A_{16}^{n,n+1}) & A_{14}^{n,n} & A_{15}^{n,n+1} & A_{17}^{n,n+1} & A_{18}^{n,n+1} \\ A_{21}^{n,n} & A_{22}^{n,n} & (A_{23}^{n,n} - A_{26}^{n,n+1}) & A_{24}^{n,n} & A_{25}^{n,n+1} & A_{27}^{n,n+1} & A_{28}^{n,n+1} \\ A_{31}^{n,n} & A_{32}^{n,n} & (A_{33}^{n,n} - A_{36}^{n,n+1}) & A_{34}^{n,n} & A_{35}^{n,n+1} & A_{37}^{n,n+1} & A_{38}^{n,n+1} \\ A_{41}^{n,n} & A_{42}^{n,n} & (A_{43}^{n,n} - A_{46}^{n,n+1}) & A_{44}^{n,n} & A_{45}^{n,n+1} & A_{47}^{n,n+1} & A_{48}^{n,n+1} \\ A_{51}^{n+1,n} & A_{52}^{n+1,n} & (A_{53}^{n+1,n} - A_{56}^{n+1,n+1}) & A_{54}^{n+1,n} & A_{55}^{n+1,n+1} & A_{57}^{n+1,n+1} & A_{58}^{n+1,n+1} \\ A_{61}^{n+1,n} & A_{62}^{n+1,n} & (A_{63}^{n+1,n} - A_{66}^{n+1,n+1}) & A_{64}^{n+1,n} & A_{65}^{n+1,n+1} & A_{67}^{n+1,n+1} & A_{68}^{n+1,n+1} \\ A_{71}^{n+1,n} & A_{72}^{n+1,n} & (A_{73}^{n+1,n} - A_{76}^{n+1,n+1}) & A_{74}^{n+1,n} & A_{75}^{n+1,n+1} & A_{77}^{n+1,n+1} & A_{78}^{n+1,n+1} \end{bmatrix} \begin{bmatrix} T_{n1} \\ T_{n2} \\ T_{n3} \\ T_{n4} \\ T_{n+1,5} \\ T_{n+1,7} \\ T_{n+1,8} \end{bmatrix}$$

In the above expression, the first letter of superscript represents the test quadrilateral and the second letter represents the source quadrilateral element. To ensure continuity of current at the common edge it is assumed that $T_{n+1,6} = -T_{n3}$. With an assembled mesh of all quadrilaterals over the surface of polygonal plate, the left side of equation (13) can be written as

$$[Z][T] \quad (16)$$

where the elements of the matrix are obtained from A_{ij}^{nm} and the column matrix $[T]$ represents the unknown amplitude of current at the edges of quadrilateral elements. Using (16) the equation (13) can be written in a matrix form

$$[Z][T] = [V] \quad (17)$$

where the elements of column vector matrix are obtained from

$$V_j = - \int_m \int_{\tan} \bar{\mathbf{B}}_{mj} \cdot [\bar{\mathbf{E}}_{in}] ds_m \quad (18)$$

The edge currents obtained after solving the matrix equation (17) are then used to determine the EM scattering from polygonal thin metallic plates. It is noted that the T_i on the boundary edges are forced to zero before solving the matrix equation (17).

Scattered Far Field:

The scattered far field due to the polygonal plate is estimated from

$$E_\theta = -jk_0\eta_0 (A_x \cos(\phi) \cos(\theta) + A_y \sin(\phi) \cos(\theta)) \quad (19)$$

$$E_\phi = -jk_0\eta_0 (-A_x \sin(\phi) + A_y \cos(\phi)) \quad (20)$$

where A_x and A_y are obtained from

$$\bar{\mathbf{A}} = \frac{e^{-jk_0r}}{4\pi \cdot r} \sum_{n=1}^N \sum_{i=1}^4 T_{ni} \iint_S \bar{\mathbf{B}}_{ni} e^{jk_0(x' \cos(\phi) \sin(\theta) + y' \sin(\phi) \sin(\theta))} ds_n \quad (21)$$

From the far fields, the radar cross sections, for co and cross polarizations are obtained as

$$\sigma_{HH} = \lim_{r \rightarrow \infty} 4\pi \cdot r^2 \frac{|E_{s\theta}|^2}{|E_{\theta_i}|^2} \quad (22)$$

$$\sigma_{HE} = \lim_{r \rightarrow \infty} 4\pi \cdot r^2 \frac{|E_{s\phi}|^2}{|E_{\theta_i}|^2} \quad (23)$$

$$\sigma_{EH} = \lim_{r \rightarrow \infty} 4\pi \cdot r^2 \frac{|E_{s\theta}|^2}{|E_{\phi_i}|^2} \quad (24)$$

$$\sigma_{EE} = \lim_{r \rightarrow \infty} 4\pi \cdot r^2 \frac{|E_{s\phi}|^2}{|E_{\phi_i}|^2} \quad (25)$$

3. NUMERICAL RESULTS

In this section the Radar Cross Section (RCS) of polygonal, thin metallic plates of various shapes is calculated using the quadrilateral meshing scheme. To validate the present analysis and the computer code developed, the numerical results obtained by the present method are compared with (1) the RCS computed using the ESP code [4], (2) the RCS computed using triangular meshing¹, and (3) the RCS measured in the Langley Experimental Test Range Facility [4].

RCS of Hexagonal Plate:

As a first example, a hexagonal plate with $a = 2.074$ cm, as shown in Figure 5, is considered. Using the hexa.SES file (listing given on the attached disk), the hexagonal plate is modeled and meshed (also shown in Figure 5 using the Geostar/COSMOS commercial software). The hexa.MOD file generated by Geostar is then imported into PoMePl (Polygonal Metallic Plate, listing given on the attached disk) electromagnetic code written in FORTRAN to estimate the RCS of polygonal, thin metallic plates. The mono-static RCS of the hexagonal plate

¹ MoM code developed at the Electromagnetic Research Branch of NASA Langley Research Center by the author.

is calculated for both E- and H-polarized incident waves for various discretization levels and is shown in Figures 6-7. It is clear from the Figures 6-7 that the discretization level with the number of edges more than 232 yields fairly consistent numerical results. Hence for the RCS computation of hexagonal plate shown in Figures 8-11 the number of edges used was 232. The Figures 8-11 also give a comparison of the results obtained using the quadrilateral meshing with the results obtained using triangular meshing, the ESP code [4], and the measured data [4]. From Figures 8-11 it can be observed that the results obtained using the quadrilateral meshing agrees well with the other numerical data as well as with the measured results. However, for E-

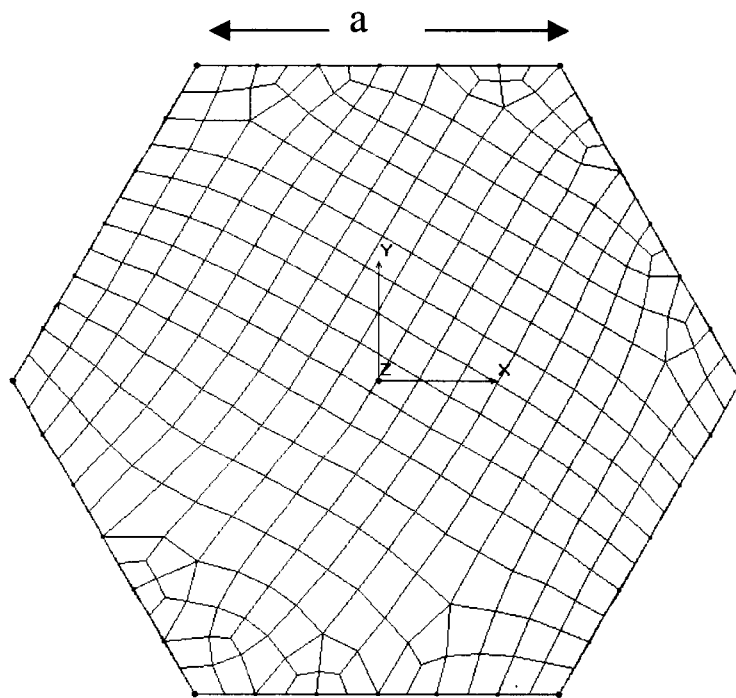


Figure 5: Thin, metallic flat plate of hexagonal shape with side $a = 2.074$ cm and discretized into quadrilateral sub-domains.

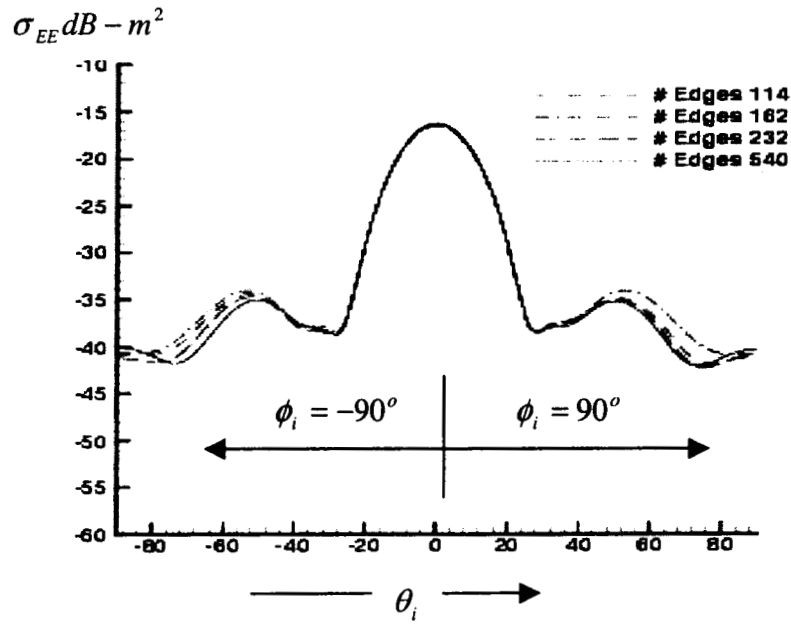


Figure 6: Monostatic RCS of hexagonal plate shown in Figure 5 when illuminated by E-polarized plane wave as a function of number of edges

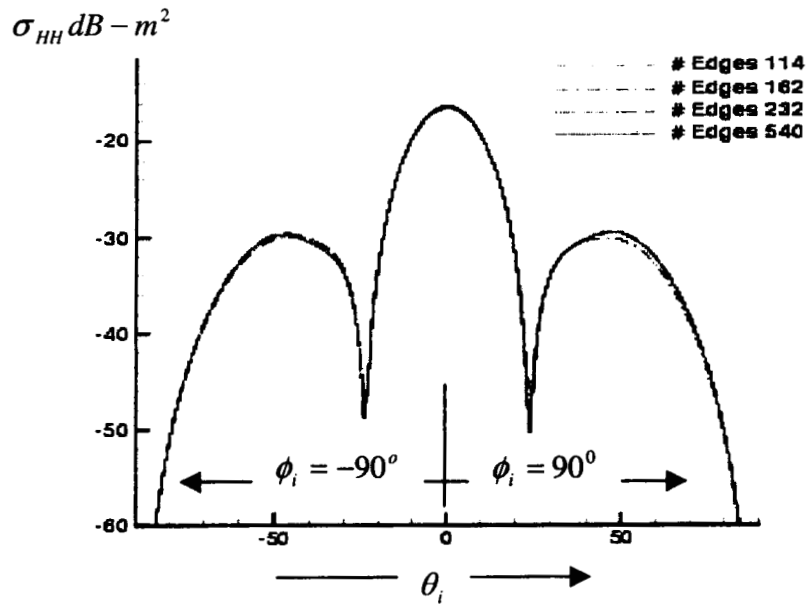


Figure 7: Monostatic RCS of hexagonal plate shown in Figure 5 when illuminated by H-polarized plane wave as a function of number of edges

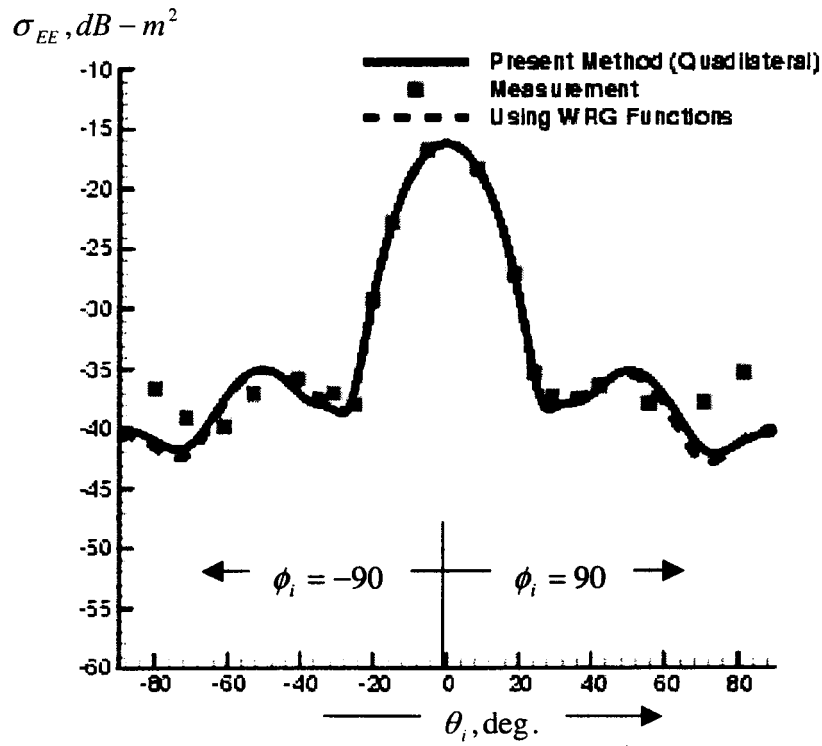


Figure 8 Monostatic RCS of hexagonal plate (shown in Figure 5) when illuminated by E-polarized plane wave $\alpha_0 = 90^\circ$ at $\phi_i = -90^\circ$ and $\phi_i = 90^\circ$, solid line- present method, dashed line RWG functions, solid square symbol- measurement, frequency = 11.811GHz.

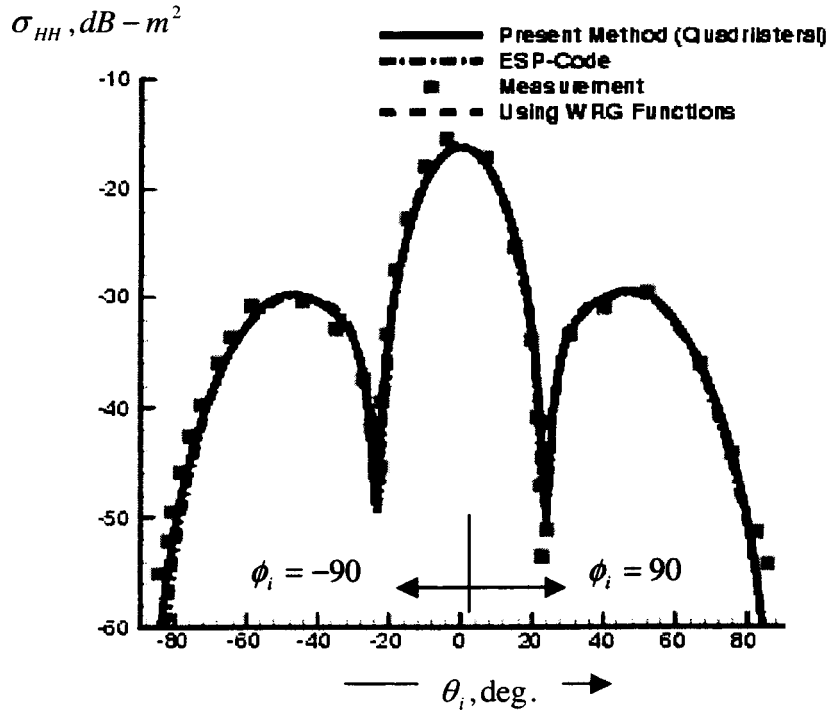


Figure 9 Monostatic RCS of hexagonal plate (shown in Figure 5) when illuminated by H-polarized plane wave $\alpha_0 = 0^\circ$ at $\phi_i = -90^\circ$ and $\phi_i = 90^\circ$, solid line- present method, dashed dot line ESP-code, solid square symbol- measurement, and dashed line RWG function, frequency = 11.811GHz.

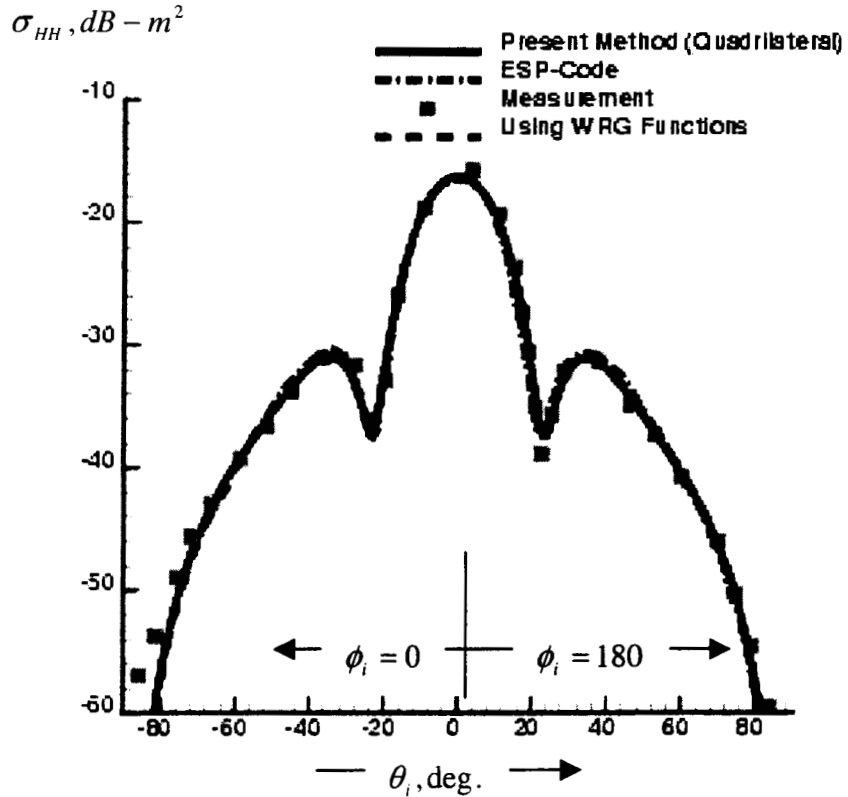


Figure 10 Monostatic RCS of hexagonal plate (shown in Figure 5) when illuminated by H-polarized plane wave $\alpha_0 = 0^\circ$ at $\phi_i = 0^\circ$ and $\phi_i = 180^\circ$, solid line- present method, dashed dot line ESP-code, solid square symbol- measurement, and dashed line RWG function, frequency = 11.811GHz.

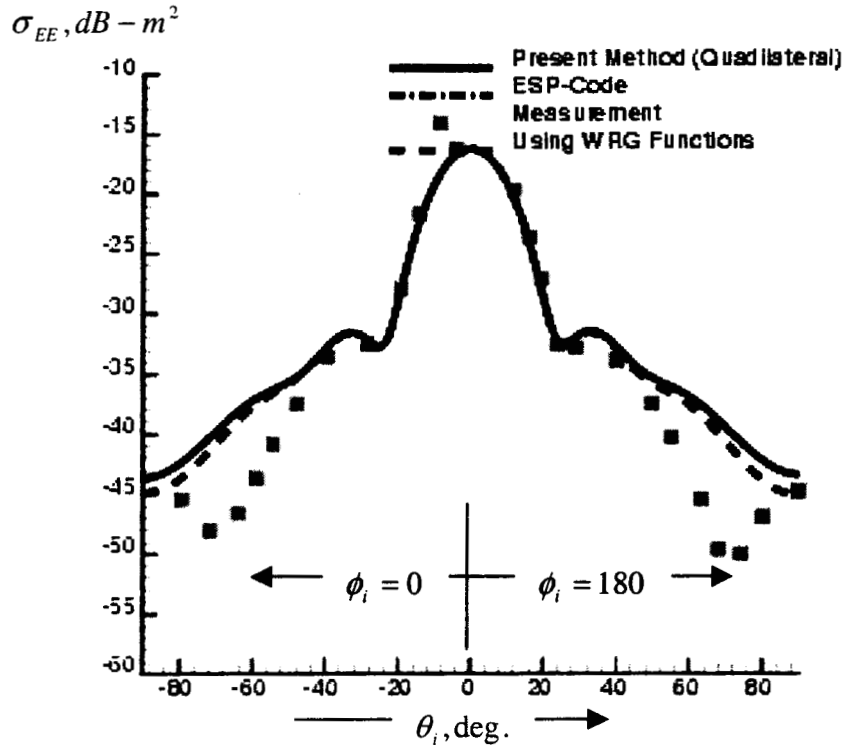


Figure 11 Monostatic RCS of hexagonal plate (shown in Figure 5) when illuminated by E-polarized plane wave $\alpha_0 = 90^\circ$ at $\phi_i = 0^\circ$ and $\phi_i = 180^\circ$, solid line- present method, dashed line RWG functions, solid square symbol- measurement, frequency = 11.811GHz

polarized incidence close to grazing angles, the computed results do not agree well with the measured data. This is due to the fact that in the computation the finite thickness of the plate is assumed to be zero.

RCS of Equilateral Triangular Plate:

A equilateral triangular plate as shown in Figure 12 is considered as a second example for the validation of the present code based on the quadrilateral meshing. Using the COSMOS/GEOSTAR the equilateral triangle is discretized into quadrilateral patches as shown in Figure 12. The *.MOD file, in conjunction with PoMePl code is used to estimate the monostatic RCS of the equilateral triangular plate. The results of the computations are shown in Figures 13-18 along with the experimental and other numerical data. The monostatic RCS

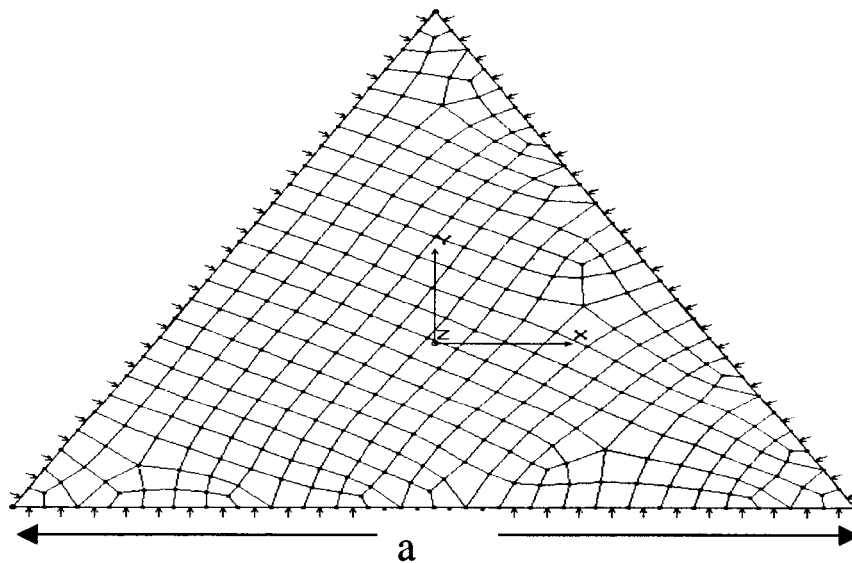


Figure 12 Equilateral triangular, thin, metallic flat plate with $a = 5.08$ cm

calculated using the quadrilateral meshing compares well with the results obtained using the triangular meshing and the ESP – code. The experimental data also compares well with the numerical data as long as the angle of incidence is not close to grazing. The discrepancy

between the measured and numerical data at angles close to grazing is because of the assumption of zero thickness in the numerical simulation. The discrepancy between measured and numerical data as a function of frequency for the grazing incident angles, as shown in Figure 17, illustrate the necessity of taking into account the thickness of the plate in the numerical simulation techniques for more accurate results.

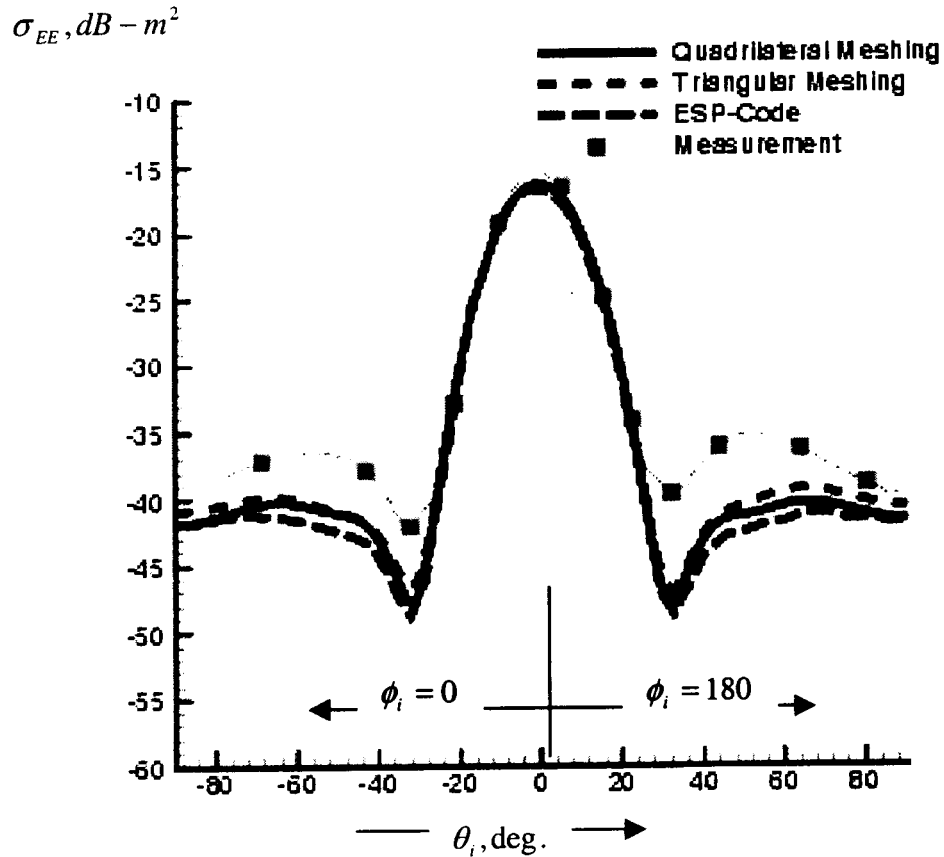


Figure 13 Monostatic RCS of equilateral triangular plate (shown in Figure 12) when illuminated by E-polarized plane wave $\alpha_0 = 90^\circ$ at $\phi_i = 0^\circ$ and $\phi_i = 180^\circ$, solid line- present method, short dashed line- RWG functions, long dashed line ESP-code, solid square symbol- measurement, frequency = 11.811GHz.

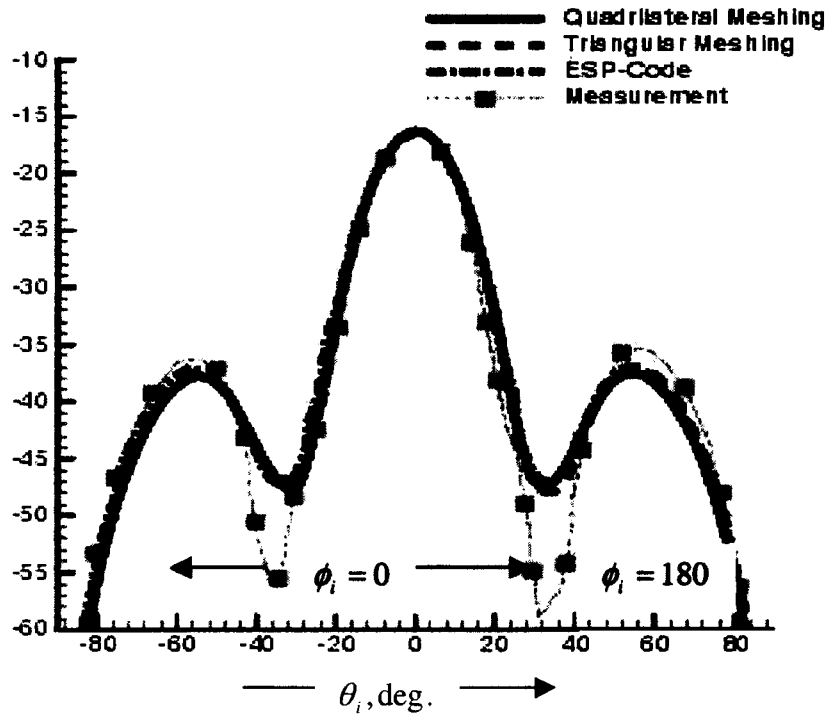


Figure 14 Monostatic RCS of equilateral triangular plate (shown in Figure 12) when illuminated by H-polarized plane wave $\alpha_0 = 0^\circ$ at $\phi_i = 0^\circ$ and $\phi_i = 180^\circ$, solid line- present method, short dashed line- RWG functions, dashed dot line ESP-code, solid square symbol- measurement, frequency = 11.811GHz

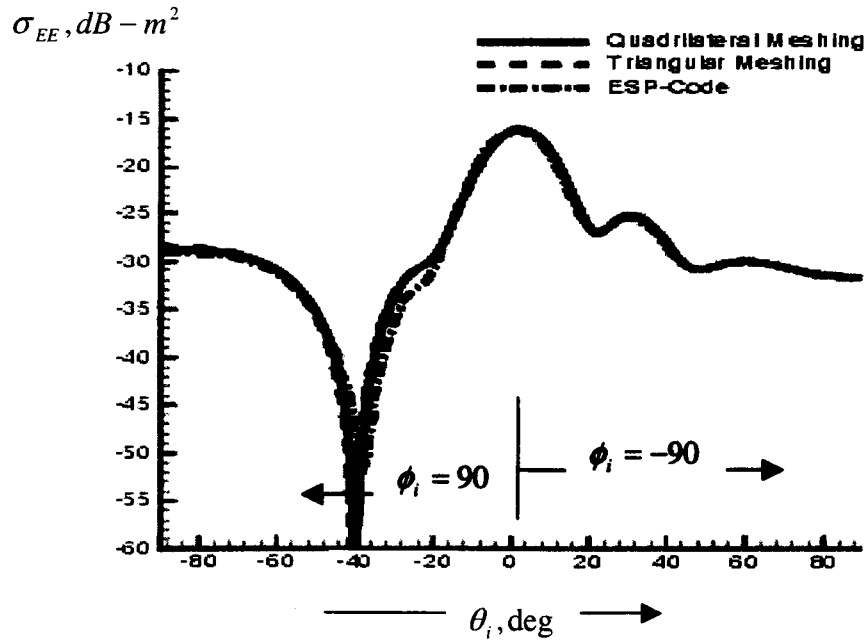


Figure 15 Monostatic RCS of equilateral triangular plate (shown in Figure 12) when illuminated by E-polarized plane wave $\alpha_0 = 90^\circ$ at $\phi_i = -90^\circ$ and $\phi_i = 90^\circ$, solid line- present method, short dashed line- RWG functions, dashed dot line ESP-code, frequency = 11.811GHz

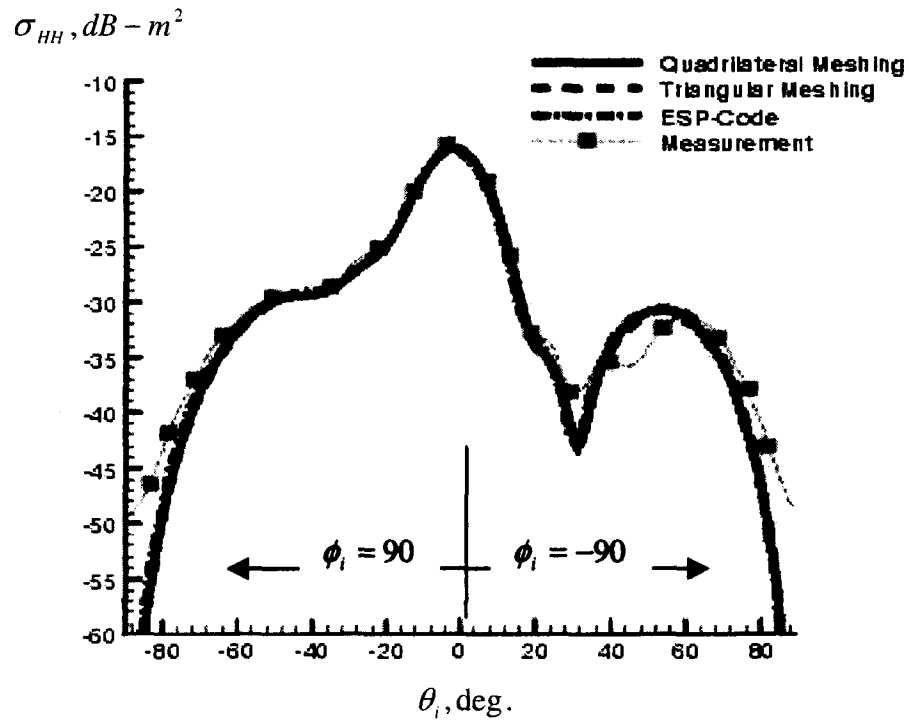


Figure 16 Monostatic RCS of equilateral triangular plate (shown in Figure 12) when illuminated by H-polarized plane wave $\alpha_0 = 0^\circ$ at $\phi_i = -90^\circ$ and $\phi_i = 90^\circ$, solid line- present method, short dashed line- RWG functions, dashed dot line ESP-code, solid square symbol- measurement, frequency = 11.811GHz.

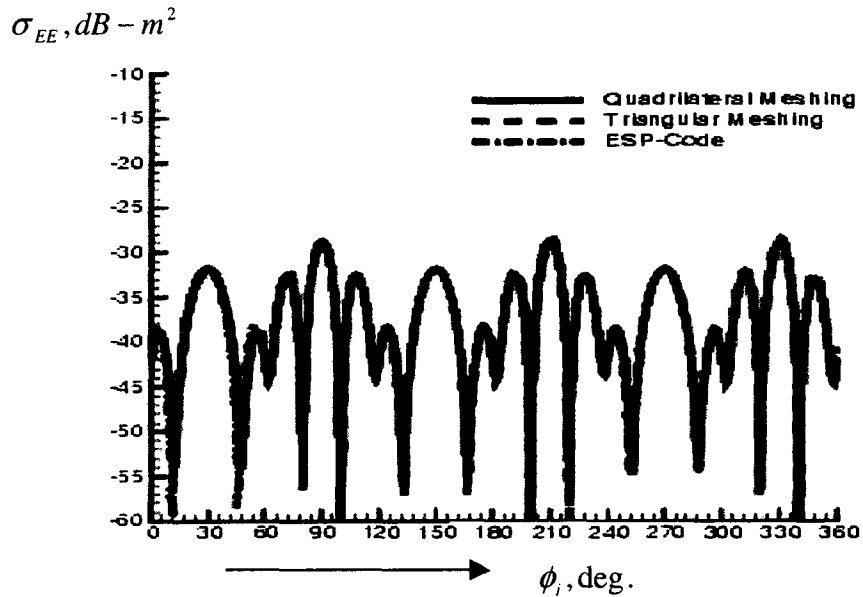


Figure 17 Monostatic RCS of equilateral triangular plate (shown in Figure 12) when illuminated by E-polarized plane wave $\alpha_0 = 90^\circ$ as a function of ϕ_i for frequency = 11.811 GHz, $\theta_i = 90^\circ$. solid line- present method, short dashed line- RWG functions, dashed dot line ESP-code, frequency = 11.811GHz.

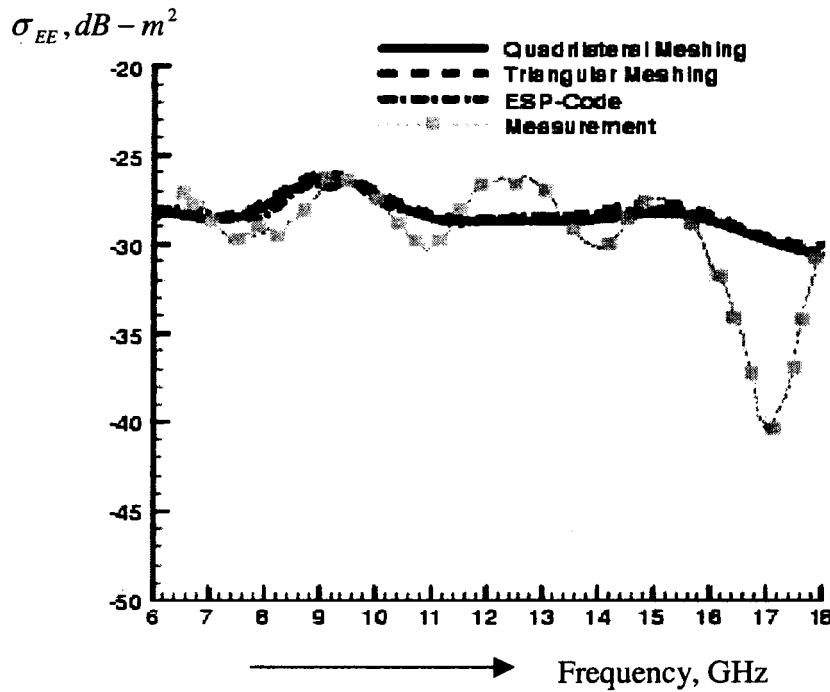


Figure 18 Monostatic RCS of equilateral triangular plate (shown in Figure 12) when illuminated by E-polarized plane wave $\alpha_0 = 90^\circ$ as a function of frequency for $\phi_i = 90$ and $\theta_i = 90^\circ$. solid line- present method, short dashed line- RWG functions, dashed dot line ESP-code, solid square symbols- measurement.

RCS of Equilateral Triangular Plate With Concentric, Equilateral Triangular Hole.

An equilateral triangular plate with a concentric equilateral triangular hole as shown in Figure 18 is considered as an another example for the validation of the present code based on the quadrilateral meshing. Using the COSMOS/GEOSTAR the equilateral triangle is discretized into quadrilateral patches as shown in Figure 18. The *.MOD file, in conjunction with PoMePl code is used to estimate the mono-static RCS of the equilateral triangular plate with an equilateral triangular hole. The results of the computations are shown in Figures 19-24 along with the experimental and other numerical data. The mono-static RCS calculated using the

quadrilateral meshing compares well with the other numerical data as well as with the experimental results.

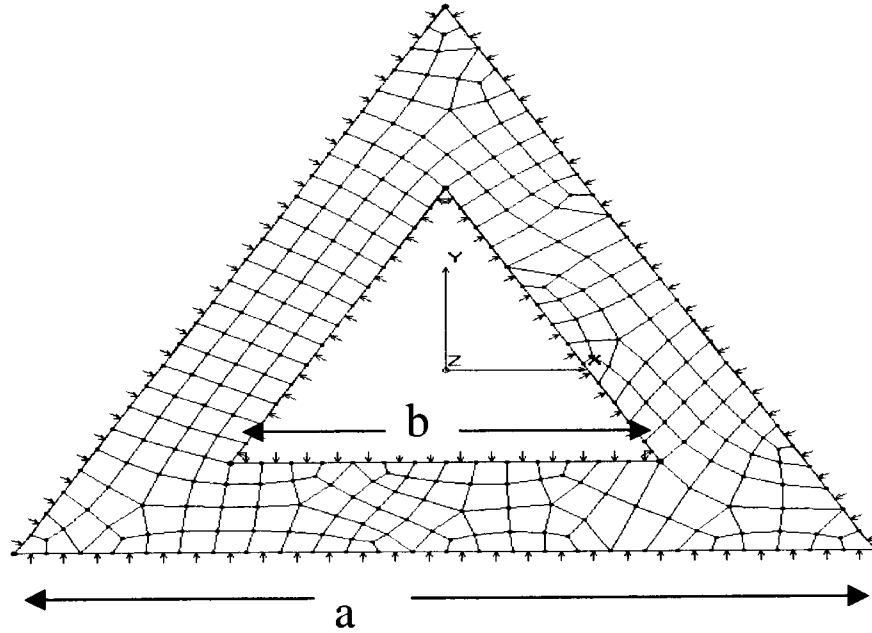


Figure 19 Equilateral triangular thin metallic flat plate with a concentric equilateral triangular hole, $a = 5.08$ cm, $b = 2.54$ cm and discretized into quadrilateral patches.

For this example, it is also observed that the numerical simulation data do not match well with the experimental results for grazing incidence.

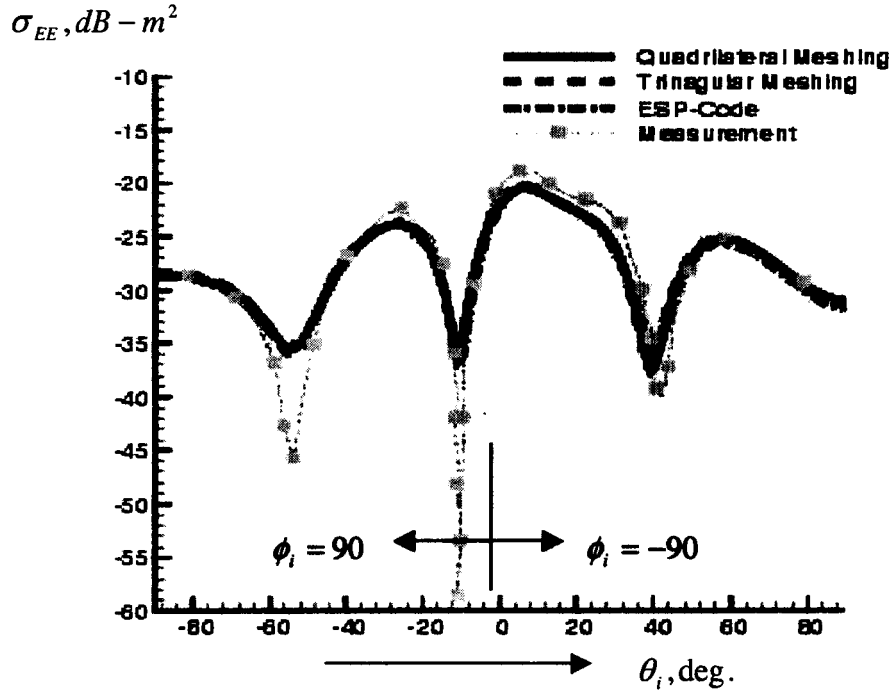


Figure 20 Monostatic RCS of equilateral triangular plate with equilateral triangular hole (shown in Figure 19) when illuminated by E-polarized plane wave $\alpha_0 = 90^\circ$ at $\phi_i = -90^\circ$ and $\phi_i = 90^\circ$, solid line- present method, short dashed line- RWG functions, dashed dot line ESP-code, solid square symbols- measurement, frequency = 11.811GHz.

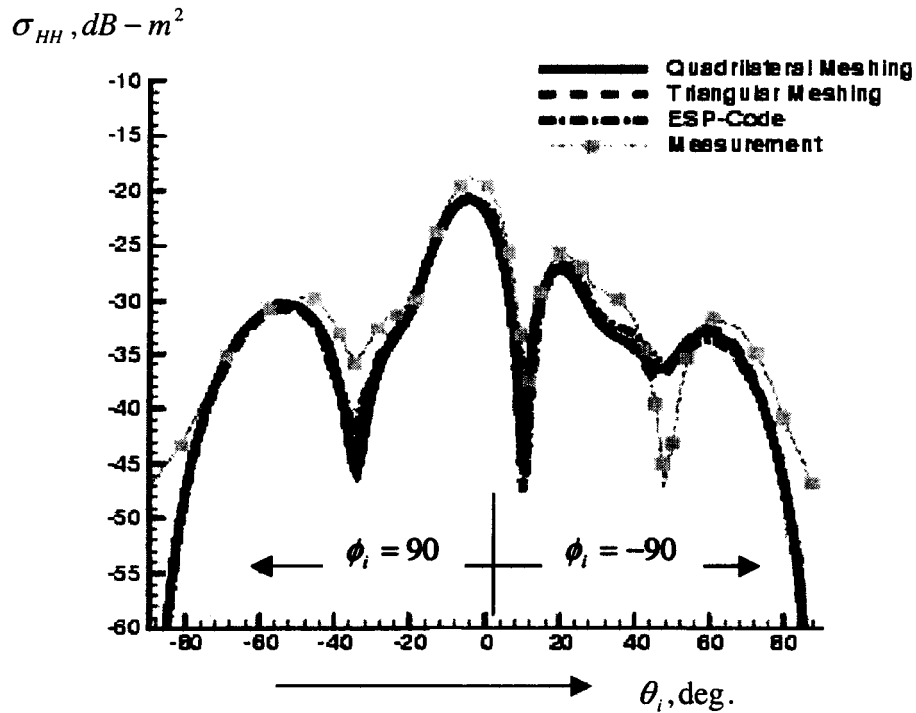


Figure 21 Monostatic RCS of equilateral triangular plate with equilateral triangular hole (shown in Figure 19) when illuminated by H-polarized plane wave $\alpha_0 = 0^\circ$ at $\phi_i = -90^\circ$ and $\phi_i = 90^\circ$, solid line- present method, short dashed line- RWG functions, dashed dot line ESP-code, solid square symbols- measurement, frequency = 11.811GHz.

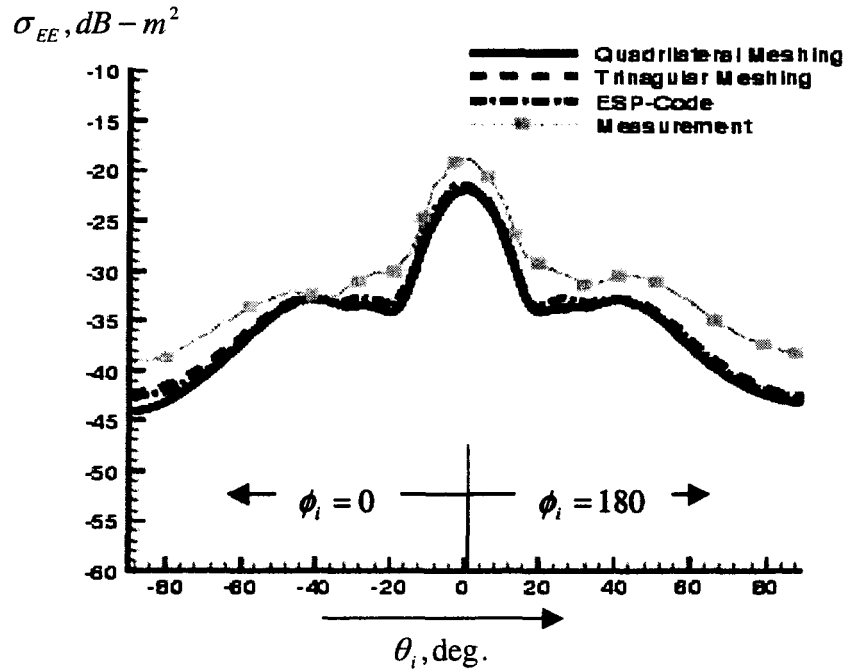


Figure 22 Monostatic RCS of equilateral triangular plate with equilateral triangular hole (shown in Figure 19) when illuminated by E-polarized plane wave $\alpha_0 = 90^\circ$ at $\phi_i = 0^\circ$ and $\phi_i = 180^\circ$, solid line- present method, short dashed line- RWG functions, dashed dot line ESP-code, solid square symbols- measurement, frequency = 11.811GHz.

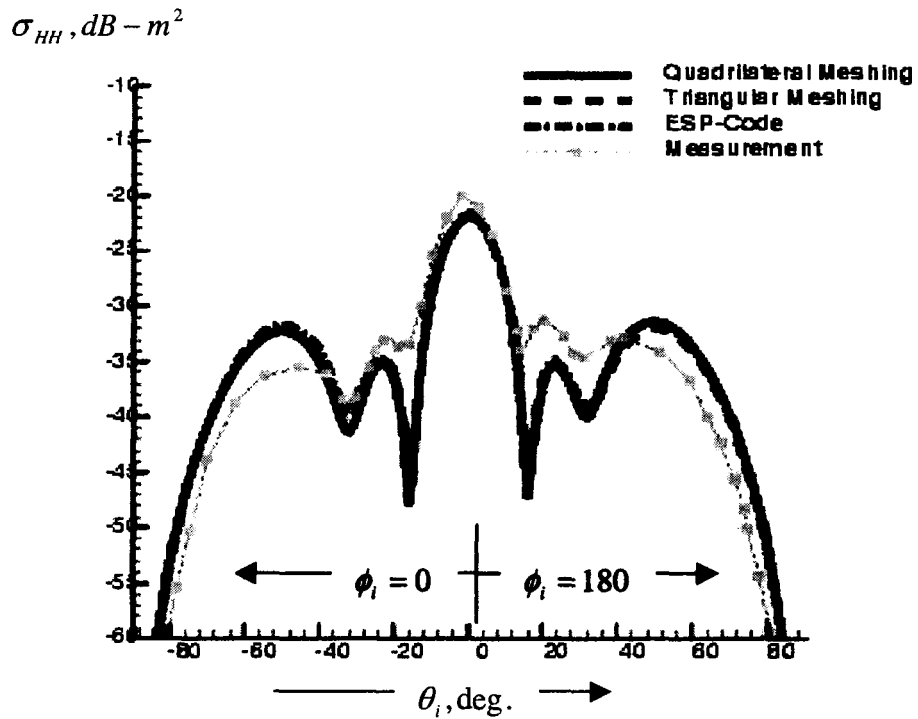


Figure 23 Monostatic RCS of equilateral triangular plate with equilateral triangular hole (shown in Figure 19) when illuminated by H-polarized plane wave $\alpha_0 = 0^\circ$ at $\phi_i = 0^\circ$ and $\phi_i = 180^\circ$, solid line- present method, short dashed line- RWG functions, dashed dot line ESP-code, solid square symbols- measurement, frequency = 11.811GHz.

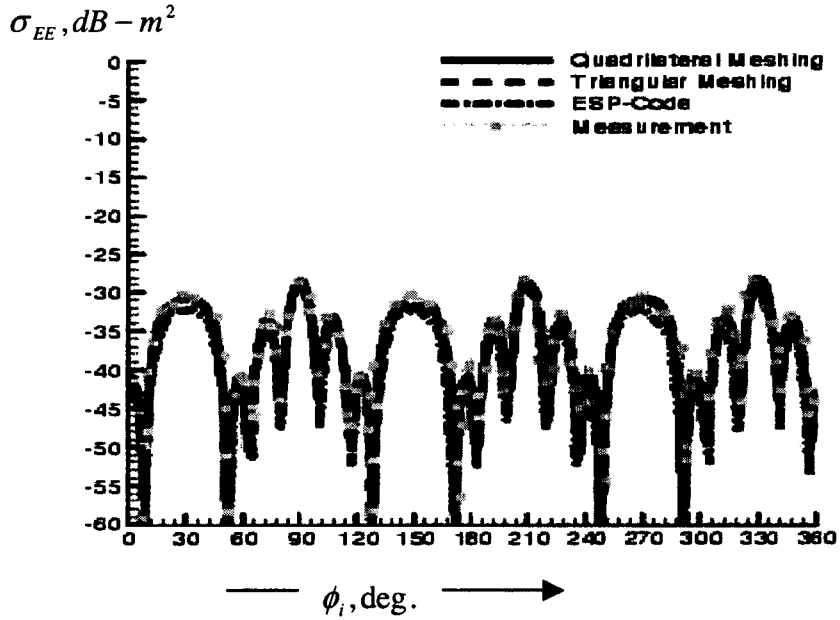


Figure 24 Monostatic RCS of equilateral triangular plate with equilateral triangular hole (shown in Figure 19) when illuminated by E-polarized plane wave $\alpha_0 = 90^\circ$ as a function of ϕ_i for frequency = 11.811 GHz, $\theta_i = 90^\circ$. solid line- present method, short dashed line- RWG functions, dashed dot line ESP-code, solid square symbols- measurement, frequency = 11.811GHz.

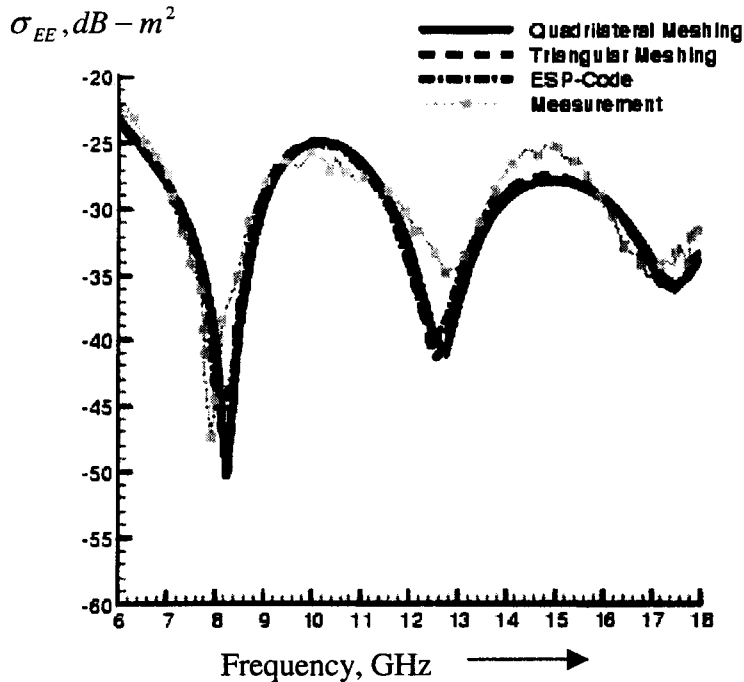


Figure 25 Monostatic RCS of equilateral triangular plate with equilateral triangular hole (shown in Figure 19) when illuminated by E-polarized plane wave $\alpha_0 = 90^\circ$ as a function of frequency for $\phi_i = -90^\circ$ and $\theta_i = 90^\circ$ (grazing incidence at edge). solid line- present method, short dashed line- RWG functions, dashed dot line ESP-code, solid square symbols- measurement

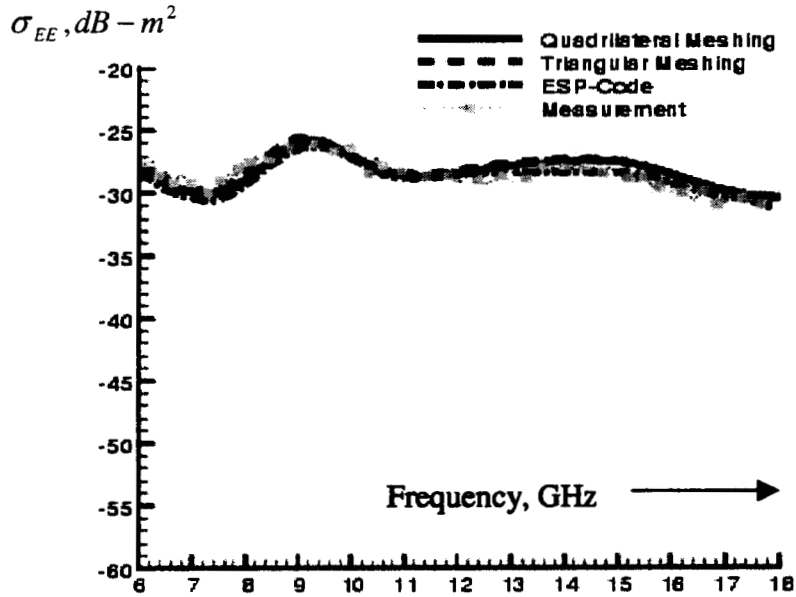


Figure 26 Monostatic RCS of equilateral triangular plate with equilateral triangular hole (shown in Figure 19) when illuminated by E-polarized plane wave $\alpha_0 = 90^\circ$ as a function of frequency for $\phi_i = 90^\circ$ and $\theta_i = 90^\circ$ (grazing incidence at tip). solid line- present method, short dashed line- RWG functions, dashed dot line ESP-code, solid square symbols- measurement

RCS of Diamond Shaped Plate

A diamond shaped polygonal plate as shown in Figure 25 is considered as a last example for validation of the present code. Using the COSMOS/GEOSTAR the diamond shaped plate is discretized into quadrilateral patches as shown in Figure 25. The *.MOD file, in conjunction with PoMePl code is used to estimate the mono-static RCS of the diamond shaped plate. The results of the computations are shown in Figures 26-30 along with the experimental and other numerical data. The mono-static RCS calculated using the quadrilateral meshing compares well with the other numerical data as well as with the experimental results. For this example, it is also observed that the numerical simulation data do not match well with the experimental results for grazing incidence.

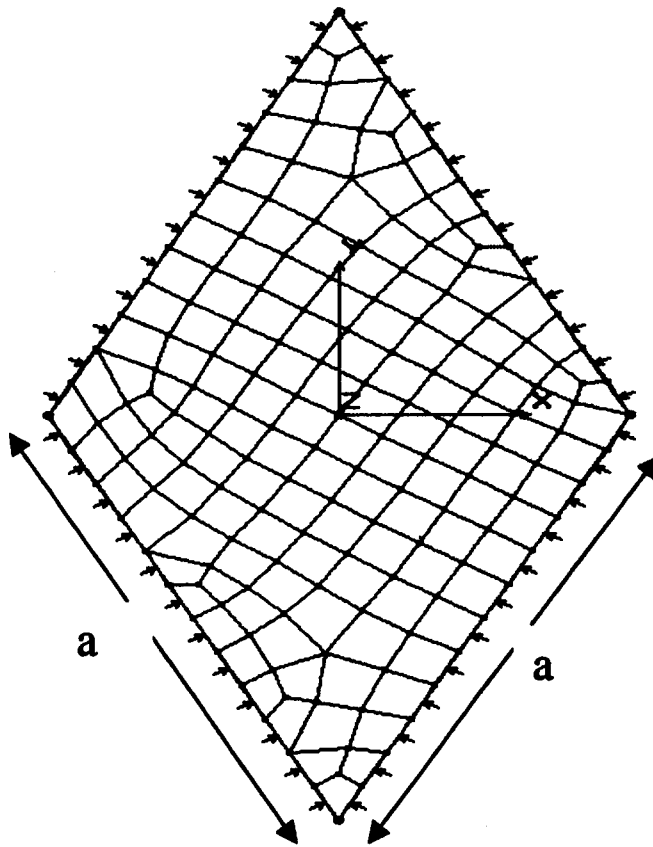


Figure 27 Thin, metallic diamond-shaped flat plate with $a = 3.592$ cm and discretized into quadrilateral patches

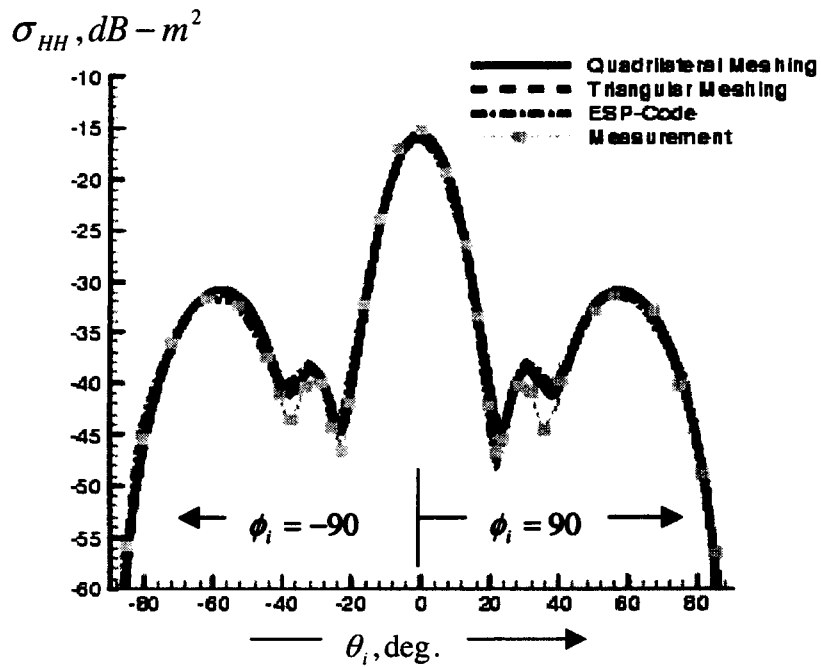


Figure 28 Monostatic RCS of diamond-shaped plate (shown in Figure 27) when illuminated by H-polarized plane wave $\alpha_0 = 0^\circ$ at $\phi_i = 90^\circ$ and $\phi_i = -90^\circ$, solid line- present method, short dashed line- RWG functions, dashed dot line ESP-code, solid square symbols- measurement, frequency = 11.811GHz.

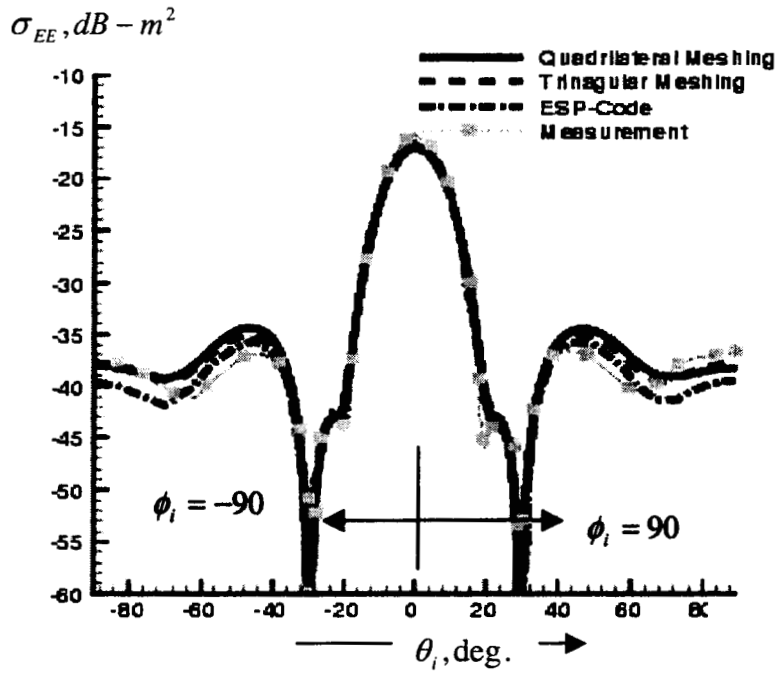


Figure 29 Monostatic RCS of diamond-shaped plate (shown in Figure 27) when illuminated by E-polarized plane wave $\alpha_0 = 90^\circ$ at $\phi_i = 90^\circ$ and $\phi_i = -90^\circ$, solid line-present method, short dashed line- RWG functions, dashed dot line ESP-code, solid square symbols- measurement, frequency = 11.811GHz.

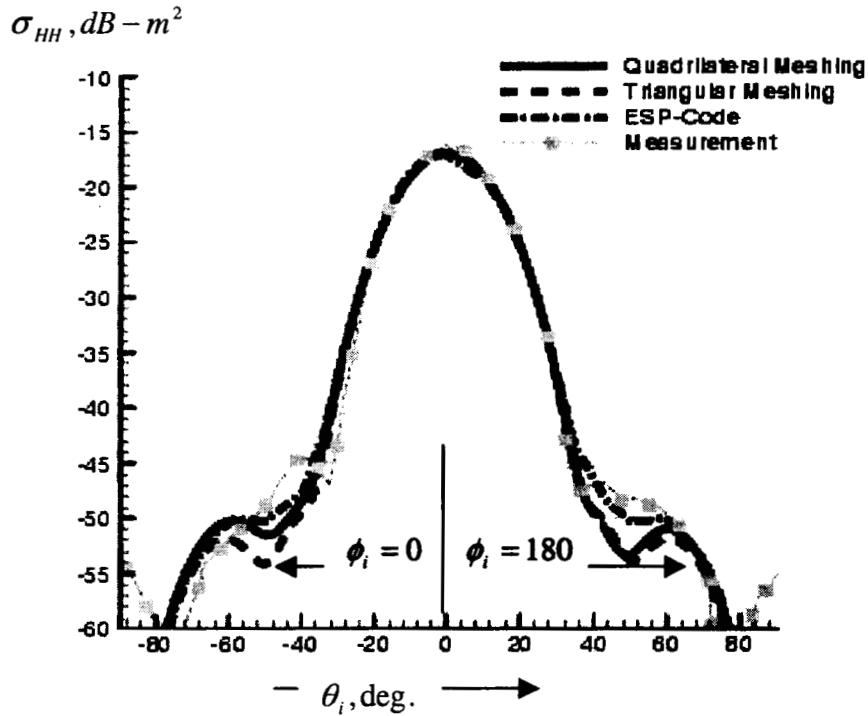


Figure 30 Monostatic RCS of diamond-shaped plate (shown in Figure 27) when illuminated by H-polarized plane wave $\alpha_0 = 0^\circ$ at $\phi_i = 0^\circ$ and $\phi_i = 180^\circ$, solid line-present method, short dashed line- RWG functions, dashed dot line ESP-code, frequency = 11.811GHz.

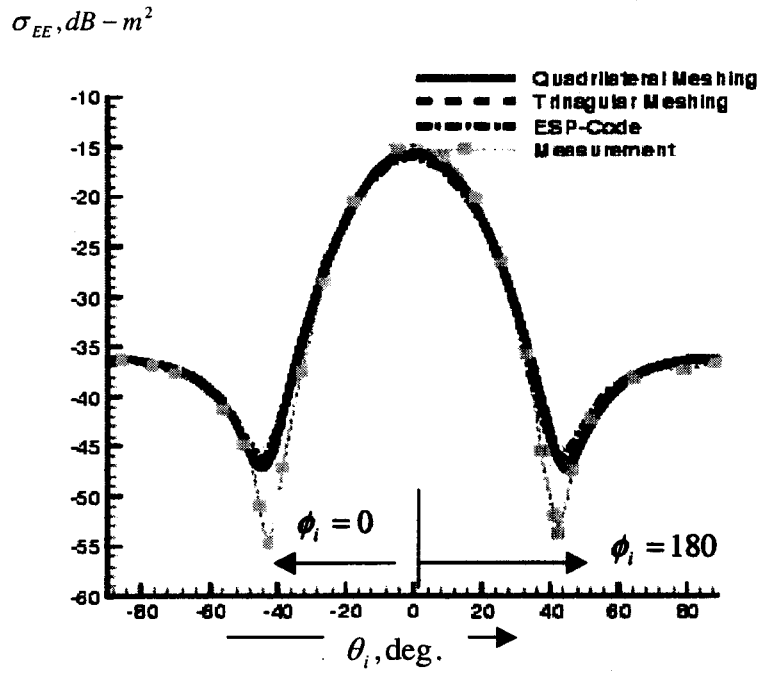


Figure 31 Monostatic RCS of diamond-shaped plate (shown in Figure 27) when illuminated by E-polarized plane wave $\alpha_0 = 90^\circ$ at $\phi_i = 0^\circ$ and $\phi_i = 180^\circ$, solid line- present method, short dashed line- RWG functions, dashed dot line ESP-code, solid square symbols- measurement, frequency = 11.811GHz.

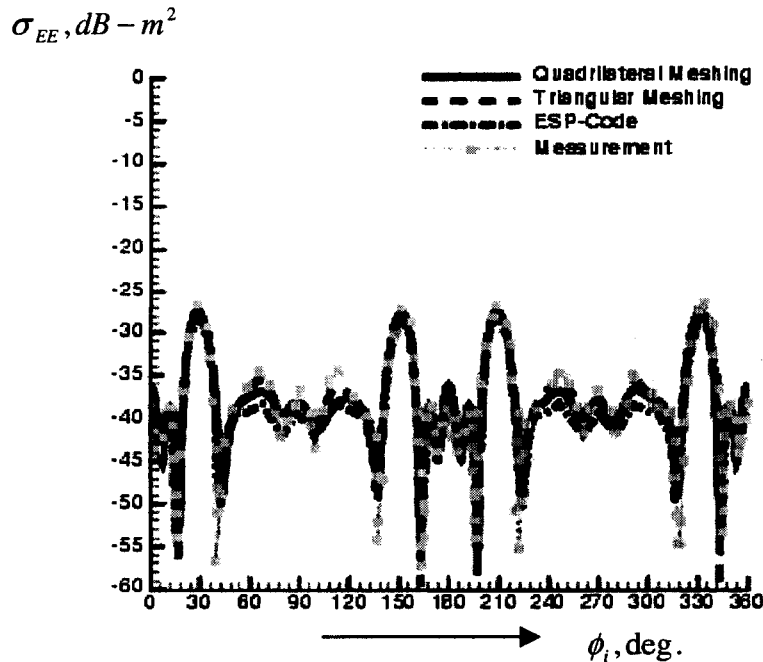


Figure 32 Monostatic RCS of diamond-shaped plate (shown in Figure 27) when illuminated by E-polarized plane wave $\alpha_0 = 90^\circ$ as a function of ϕ_i for frequency = 11.811 GHz, $\theta_i = 90^\circ$. solid line- present method, short dashed line- RWG functions, dashed dot line ESP-code, solid square symbols- measurement, frequency = 11.811GHz.

4 CONCLUSION

The electric field integral equation approach in conjunction with the method of moments with quadrilateral meshing has been described to estimate the electromagnetic scattering from irregularly shaped thin metallic plates. Discretizing an irregularly shaped thin plate into quadrilateral patches and using proper expansion and testing functions over the quadrilateral sub-domains, the integral equation has been reduced to a matrix equation. From the knowledge of the surface currents density, obtained after solving the matrix equation, the EM scattering from various irregularly shaped plates has been determined and compared with earlier published results. The novelty in the present approach is the use of quadrilateral patches instead of well known and often used triangular patches. It has been observed that the use of quadrilateral patches instead of triangular patches reduces the number of unknowns and hence it requires handling of reduced size matrices. Also, the quadrilateral patches are more natural to satisfy the boundary edge currents condition, i.e., zero normal component compared to the triangular patches. This property makes it possible to achieve convergent results fewer quadrilateral patches.

The numerical results obtained using quadrilateral patches have been compared with the numerical results obtained using the triangular patches and ESP-code. The numerical results obtained by the present code have also been compared with the measured data obtained in the NASA Langley Experimental Test Range Facility.

APPENDIX A

Construction of the vector basis function $\vec{B}_{ni}(x, y)$ for an arbitrarily shaped quadrilateral in the x-y coordinate system is a complex problem. However, a coordinate transformation that

transforms a quadrilateral in the x-y plane into a square element in a new (ξ, η) coordinates plane simplifies the derivation as shown below. Using the following transformation

$$x = \sum_{i=1}^4 N_i(\xi, \eta) x_i \text{ and } y = \sum_{i=1}^4 N_i(\xi, \eta) y_i \quad (\text{A1})$$

where

$$N_1 = \frac{1}{4}(1-\xi)(1-\eta), \quad N_2 = \frac{1}{4}(1-\xi)(1+\eta), \quad N_3 = \frac{1}{4}(1+\xi)(1+\eta), \text{ and } N_4 = \frac{1}{4}(1+\xi)(1-\eta)$$

With the coordinate transformation given in (A1), the n^{th} quadrilateral is transformed into a square with sides equal to 2, as shown in Figure 3. The vector basis function \bar{N}_i along the edges of the quadrilateral can be shown to be [6]

$$\bar{N}_1 = \frac{l_1}{4}(1-\xi)\nabla\eta, \quad \bar{N}_2 = \frac{l_2}{4}(1+\eta)\nabla\xi, \quad \bar{N}_3 = -\frac{l_3}{4}(1+\xi)\nabla\eta, \quad \bar{N}_4 = -\frac{l_4}{4}(1-\eta)\nabla\xi \quad (\text{A2})$$

If \hat{n} is the unit normal vector to the n^{th} quadrilateral, then the basis function representing the surface current can be written as

$$\bar{B}_{n1}(\xi, \eta) = \frac{l_1}{4}(1-\xi)\hat{n} \times \nabla\eta \quad \bar{B}_{n2}(\xi, \eta) = \frac{l_2}{4}(1+\eta)\hat{n} \times \nabla\xi \quad (\text{A3})$$

$$\bar{B}_{n3}(\xi, \eta) = -\frac{l_3}{4}(1+\xi)\hat{n} \times \nabla\eta \quad \bar{B}_{n4}(\xi, \eta) = -\frac{l_4}{4}(1-\eta)\hat{n} \times \nabla\xi \quad (\text{A4})$$

where the various quantities appearing in the above expressions can be expressed as [6]

$$\nabla\xi = (\hat{x}\frac{\partial y}{\partial\eta} - \hat{y}\frac{\partial x}{\partial\eta})/\det[J], \quad \nabla\eta = (-\hat{x}\frac{\partial y}{\partial\xi} + \hat{y}\frac{\partial x}{\partial\xi})/\det[J] \quad (\text{A5})$$

$$\det[J] = \frac{\partial x}{\partial\xi}\frac{\partial y}{\partial\eta} - \frac{\partial x}{\partial\eta}\frac{\partial y}{\partial\xi} \quad (\text{A6})$$

With simple mathematical manipulation it can be shown that

$$\nabla \bullet \bar{B}_{ni}(\xi, \eta) = \frac{l_i}{4} \frac{1}{\det[J]} \quad (\text{A7})$$

REFERENCES

- [1] E. H. Newman and R. J. Marhefka, " Overview of MM and UTD methods at the Ohio State University," Proc. IEEE, Vol. 77, no. 5, May 1989, pp. 700-708.
- [2] E. H. Newman and T. Pravit, " A surface patch model for polygonal plates, " IEEE Trans. On Antennas and Propagation, Vol. AP-30, no 4, July 1982, pp.588-593
- [3] S. M. Rao, D. R. Wilton, and A. W. Glisson, "Electromagnetic scattering by surfaces of arbitrary shape, " IEEE Trans. On Antennas and Propagation , Vol. AP-30, no. 3, pp. 409-418, May 1982.
- [4] M. D. Deshpande et al., "Analysis of electromagnetic scattering from irregularly shaped, thin, metallic plates, " NASA Technical Paper 3361, Oct. 1993.
- [5] E. H. Newman, "A User's manual for the electromagnetic surface patch code: ESP: Version IV, Electroscience Lab, Ohio State University, 1988.
- [6] J. Jin, "*The finite element method in electromagnetics*," John Wiley & Sons, Inc., New York, 1993

REPORT DOCUMENTATION PAGE			Form Approved OMB No. 0704-0188	
Public reporting burden for this collection of information is estimated to average 1 hour per response, including the time for reviewing instructions, searching existing data sources, gathering and maintaining the data needed, and completing and reviewing the collection of information. Send comments regarding this burden estimate or any other aspect of this collection of information, including suggestions for reducing this burden, to Washington Headquarters Services, Directorate for Information Operations and Reports, 1215 Jefferson Davis Highway, Suite 1204, Arlington, VA 22202-4302, and to the Office of Management and Budget, Paperwork Reduction Project (0704-0188), Washington, DC 20503.				
1. AGENCY USE ONLY (Leave blank)		2. REPORT DATE May 2003		3. REPORT TYPE AND DATES COVERED Technical Memorandum
4. TITLE AND SUBTITLE Electromagnetic Scattering From a Polygonal Thin Metallic Plate Using Quadrilateral Meshing			5. FUNDING NUMBERS 706-31-41-01-00	
6. AUTHOR(S) Manohar D. Deshpande				
7. PERFORMING ORGANIZATION NAME(S) AND ADDRESS(ES) NASA Langley Research Center Hampton, VA 23681-2199			8. PERFORMING ORGANIZATION REPORT NUMBER L-18272	
9. SPONSORING/MONITORING AGENCY NAME(S) AND ADDRESS(ES) National Aeronautics and Space Administration Washington, DC 20546-0001			10. SPONSORING/MONITORING AGENCY REPORT NUMBER NASA/TM-2003-212165	
11. SUPPLEMENTARY NOTES				
12a. DISTRIBUTION/AVAILABILITY STATEMENT Unclassified-Unlimited Subject Category 34 Distribution: Nonstandard Availability: NASA CASI (301) 621-0390			12b. DISTRIBUTION CODE	
13. ABSTRACT (Maximum 200 words) The problem of electromagnetic (EM) scattering from irregularly shaped, thin, metallic flat plates in free space is solved using the electric field integral equation (EFIE) approach in conjunction with the method of moments (MoM) with quadrilateral meshing. An irregularly shaped thin plate is discretized into quadrilateral patches and the unknown electric surface current over the plate is expressed in terms of proper basis functions over these patches. The basis functions for the electric surface current density that satisfy the proper boundary conditions on these quadrilateral patches are derived. The unknown surface current density on these quadrilateral patches is determined by setting up and solving the electric field integral equation by the application of the MoM. From the knowledge of the surface current density, the EM scattering from various irregularly shaped plates is determined and compared with the earlier published results. The novelty in the present approach is the use of quadrilateral patches instead of well known and often used triangular patches. The numerical results obtained using the quadrilateral patches compare favorably with measured results.				
14. SUBJECT TERMS Electromagnetic Scattering; Moment Method; Polygonal Plates			15. NUMBER OF PAGES 41	
			16. PRICE CODE	
17. SECURITY CLASSIFICATION OF REPORT Unclassified	18. SECURITY CLASSIFICATION OF THIS PAGE Unclassified	19. SECURITY CLASSIFICATION OF ABSTRACT Unclassified	20. LIMITATION OF ABSTRACT UL	